Master's Thesis

Impact Localization in Thin-Walled Steel Structures Using Time Reversal of Guided Ultrasonic Waves

Nikolaos Papanikolaou

Delft University of Technology

TU Delft

Master's Thesis

Impact Localization in Thin-Walled Steel Structures Using Time Reversal of Guided Ultrasonic Waves

by

Nikolaos Papanikolaou

to obtain the degree of Master of Science in Offshore and Dredging Engineering
to be defended publicly on September 1, 2025.

Thesis exam committee:

Chair:	Dr. L. Pahlavan
Committee Members:	Dr. L. Pahlavan
	Ir. C. Saccone
	Prof. Dr. C. Kassapoglou
	Dr. Ir. P.R. Wellens
	Ir. J.A.A. Vaders

Supervisors:	Dr. L. Pahlavan
	Ir. C. Saccone
Faculty:	Mechanical Engineering

Author details:

Student Number:	6067476

Acknowledgements

First and foremost, I would like to express my deep gratitude to my supervisor, Associate Professor Pooria Pahlavan for giving me the opportunity to work on the impact localization project. His positive mindset, mentorship and openness to discussion helped me grow not only as a researcher but also as a person. Furthermore, I am grateful to Cecilia Saccone, my daily supervisor, for her guidance, assistance, feedback and encouragement throughout the duration of the project.

This research could not have been realized to this extent without the support of Andre Vaders from COMMIT and Robin van Dijke and Juri Kuzjatkin from DAMEN, who showed genuine interest in my research and supported me both in the arrangement and execution of the large scale experiments.

In addition, I want to thank my friends, both the old ones from my school years and the new ones I made in the Netherlands, for always being available to express my concerns to, and emotionally support me through challenging times. I also want to express a heartfelt thanks to my girlfriend Michaela for the patience she showed while listening to me and for her constant support and motivation. Last but not least, I would like to deeply thank my family for their unconditional love, support and encouragement.

Finally, I express my sincere appreciation to Eugenides Foundation. Their scholarship made me realize my goal of studying abroad and allowed me to stay focused on my studies.

Nikolaos Papanikolaou
Delft, August 2025

Abstract

Offshore support and naval vessels operate in complex and hazardous environments facing the risk of impact from falling objects, collisions and projectiles. Accurate impact localization is essential to guarantee safety of the individuals, the environment and the asset.

This thesis explores the feasibility of impact localization on steel plates and stiffened panels by utilizing the information carried by the stress waves generated during impacts. These waves propagate along the surface of the structure as Guided Ultrasonic Waves (GUW). The inherent time reversibility and spatial reciprocity properties of the wave equations allow the use of Time Reversal (TR) process of the recorded wave signals to localize impacts.

The study combines experimental testing with an analytical framework. Small scale controlled impact experiments were performed in the Structures Laboratory at TU Delft while large scale tests were conducted onboard a Shoalbuster at DAMEN Shipyards in Gorinchem, allowing the assessment of the scalability and robustness of the method. Acoustic Emissions (AE) were generated through Pencil Lead Breaks (PLBs) and instrumented hammer impacts. TR was implemented virtually in the frequency domain using an analytical propagation formulation that models dispersion and wave amplitude decay due to geometric spreading. The novelty of the present research lies in extending the analytical TR framework from plates to stiffened panels by removing the effect of stiffeners in back-propagation. This is achieved by introducing a scalar transmission coefficient T_c into the analytical model.

In the small scale experiments two configurations were tested, a plate and a stiffened plate with a stiffener located at the midspan, both measuring 400 x 400 mm^2. The average localization error for the plate ranged from 11 to 15 mm, while stiffened panel tests showed slightly higher errors in the order of 12 to 23 mm, depending on the impact type. Higher errors were observed for the instrumented hammer impacts. In the large scale tests a 7500 x 2000 mm^2 area was monitored. Localization accuracy decreased due to increased structural complexity, including variable plate thickness, multiple stiffeners, and high acoustic noise from parallel steel work activity. A mean localization error of 662 mm was achieved, demonstrating the method's scalability and potential for real world application.

These results confirm that TR of GUW is a feasible method for impact localization across different scales. The methodology shows potential for extension to composite materials and towards a complete impact identification framework that includes impact severity estimation, contributing to the development of integrated Structural Health Monitoring (SHM) systems capable of detecting, localizing, and quantifying structural impacts.

Contents

List of Figures

List of Tables

Nomenclature

Abbreviations

Abbreviation	Definition
A0 / S0 / SH0	Fundamental antisymmetric, symmetric, and shear-horizontal guided-wave modes
AE	Acoustic Emission(s)
AMSY-6	Vallen acoustic emission data acquisition system
BVID	Barely Visible Impact Damage
CWT	Continuous Wavelet Transform
DAQ / DAS	Data Acquisition System
FE	Finite Element
FFT	Fast Fourier Transform
GUW	Guided Ultrasonic Waves
IEPE	Integrated Electronics Piezo-Electric
IRF	Impulse Response Function
NDT	Non Destructive Testing
PCM	Phase Conjugate Mirror
PLB	Pencil Lead Break
PZT	Lead Zirconate Titanate (piezoelectric sensor)
SHM	Structural Health Monitoring
SLDV	Scanning Laser Doppler Vibrometer
T_c	Transmission Coefficient
TDDT	Time Distance Domain Transform
ToF	Time of Flight
TR	Time Reversal
TRM	Time Reversal Mirror

1 Introduction

1.1. Background and Motivation

Managing impacts on maritime structures is a major concern in ship design and operation. Vessels operating in complex and hazardous environments, such as offshore support ships or naval vessels face the risk of impacts caused by unpredictable factors such as collisions with other marine structures, falling objects, or projectiles. The energy delivered during the impact is dissipated through several mechanisms including conversion to heat, plastic deformation, sound generation, structural vibration and the propagation of elastic waves. Impacts usually lead to severe structural, environmental and operational consequences. Therefore, accurate impact identification, is critical to ensure the safety of the individuals, the asset and the environment and also to decide whether the operation should continue or not. Impact identification consists of both determining the event's location and estimating its magnitude. This work focuses specifically on impact localization.

Traditional inspection methods, such as Non-Destructive Testing (NDT) and visual inspections, often fall short in the complex scenarios where these vessels operate due to limited accessibility to structural components or the urgency of operational schedules. This has led to increased interest in Structural Health Monitoring (SHM), which employs sensor networks to monitor structural responses in real-time and assess structural integrity without invasive tests [1].

Among the techniques utilized in SHM, Acoustic Emission (AE) is of high value for detecting sudden stress releases, such as those caused by crack initiation or growth and impacts. These stress waves propagate through thin-walled structures as Guided Ultrasonic Waves (GUW). GUW have already proven their effectiveness in monitoring large-scale structures such as bridges [2, 3, 4], offshore platforms [5, 6, 3], and pipelines [7]. However, their application to ship structures is limited. These elastic waves are confined within the geometric boundaries of thin-walled structures and can travel over large distances while carrying valuable information on the AE source characteristics. Ship hulls are mainly composed of steel plates with stiffeners, the existence of the latter introduces complexity such as, wave reflection, scattering and mode conversion, and therefore the applicability of traditional impact localization techniques is further limited.

1.2. Thesis Layout

This report explores the potential of using GUW for impact localization on steel stiffened panels such as those found in ship hulls.

Chapter 1 outlines the motivation of the work, introduces the basic theory of guided waves and explains the fundamentals of SHM using GUW. The state-of-the-art localization methods are also reviewed and their efficiency and applicability in ship structures is evaluated. Last but not least, the knowledge gaps are identified and the research questions are formulated.

Chapter 2 describes the approach followed in this study. The methodology consists of two parts. First impact experiments while monitoring AE are carried out and then an analytical model the recorded is

used to process the recorded signals localize impact.

Chapter 3 presents the experimental work carried out in the Structures Laboratory of the Mechanical Engineering faculty at TU Delft and the the large scale experiments carried out at DAMEN Shipyards in Gorinchem.

Chapter 4 details the virtual TR implementation performed in MATLAB for source localization.

Chapter 5 presents the impact localization results and their interpretation.

Chapter 6 concludes the findings of the present research and discusses the recommendations for future work and how the current methodology can be extended for complete impact identification.

1.3. Background

1.3.1. Wave Propagation in Elastic Media

The theory of elastic wave propagation has been well documented in Doyle [8] and Giurgiutiu [9]. For completeness, the fundamentals of elastic wave propagation are briefly outlined here.

The equation of motion of an elastic medium, also known as Navier equation is given in Eq. 1.1.

$$\mu\nabla^2 u + (\lambda+\mu)\nabla\nabla\cdot u = \rho\frac{\partial^2 u}{\partial t^2} \tag{1.1}$$

where, $\lambda = \frac{\nu E}{(1+\nu)(1-2\nu)}$ and $\mu = \frac{E}{2(1+\nu)}$ are the Lame constants, ρ is the material density, E is the Young's modulus, ν is Poisson ratio and u is the particle displacement vector. Equation 1.1, is in compact form and can be expanded at its three spatial components in Eq. 1.2.

$$\begin{aligned}
\mu\left(\frac{\partial^2}{\partial x^2}+\frac{\partial^2}{\partial y^2}+\frac{\partial^2}{\partial z^2}\right)u_x + (\lambda+\mu)\frac{\partial}{\partial x}\left(\frac{\partial u_x}{\partial x}+\frac{\partial u_y}{\partial y}+\frac{\partial u_z}{\partial z}\right) &= \rho\frac{\partial^2 u_x}{\partial t^2}\\
\mu\left(\frac{\partial^2}{\partial x^2}+\frac{\partial^2}{\partial y^2}+\frac{\partial^2}{\partial z^2}\right)u_y + (\lambda+\mu)\frac{\partial}{\partial x}\left(\frac{\partial u_x}{\partial x}+\frac{\partial u_y}{\partial y}+\frac{\partial u_z}{\partial z}\right) &= \rho\frac{\partial^2 u_y}{\partial t^2}\\
\mu\left(\frac{\partial^2}{\partial x^2}+\frac{\partial^2}{\partial y^2}+\frac{\partial^2}{\partial z^2}\right)u_z + (\lambda+\mu)\frac{\partial}{\partial x}\left(\frac{\partial u_x}{\partial x}+\frac{\partial u_y}{\partial y}+\frac{\partial u_z}{\partial z}\right) &= \rho\frac{\partial^2 u_z}{\partial t^2}
\end{aligned} \tag{1.2}$$

The governing wave equation can be decomposed into two uncoupled equations, using the displacement potentials method based on Helmholtz decomposition.The displacement field u is then expressed as the sum of the gradient of a scalar potential $\nabla\Phi$ and a vector potential H representing the compressional and the rotational component of the displacement field respectively, as shown in Eq.1.3.

$$u = \nabla\Phi + \nabla\times H \tag{1.3}$$

The decoupled governing equations are given in the following equations.

$$\frac{\partial^2\Phi}{\partial x^2}+\frac{\partial^2\Phi}{\partial y^2} = \frac{1}{c_P^2}\ddot{\Phi} \tag{1.4}$$

$$\frac{\partial^2 H}{\partial x^2}+\frac{\partial^2 H}{\partial y^2} = \frac{1}{c_S^2}\ddot{H} \tag{1.5}$$

where, $c_P^2 = (\lambda+\mu)/\rho$ and $c_S^2 = \mu/\rho$ are the longitudinal and shear wave speed respectively.

Assuming harmonic wave propagation in the x-direction and choosing the H potential in quadrature with the Φ potential through the factor i, the general solution to Eq. 1.4 and Eq. 1.5 is found in Eq. 1.6.

$$\Phi = f(y)e^{i(\xi x-\omega t)} \qquad H = ih(y)e^{i(\xi x-\omega t)} \tag{1.6}$$

1.3.2. Elastic waves in plates

Elastic waves in plates propagate as Guided Ultrasonic Waves. These waves are confined between the upper and lower boundary of thin-walled structures and propagate along its free surfaces, allowing for long-range propagation. This confinement is why they are referred to as "Guided". The term "Ultrasonic" refers to the high frequency of the waves, which exceeds 20 kHz. GUW propagate in different wave modes depending on the variation between the wave frequency, the material properties, and the geometry of the structure (e.g., thickness of the plate). This leads to distinct patterns of particle motion and stress distribution, each satisfying the boundary conditions and wave equations uniquely. In thin plates they fall into two categories:

- Shear Horizontal (SH) waves
- Lamb waves

Shear Horizontal (SH) waves

The particle motion of SH waves is horizontally polarized, parallel to the plate surface and perpendicular to the direction of the wave propagation as illustrated in Figure 1.1. SH waves do not involve volumetric changes, therefore the term $\nabla \cdot u$ in Eq. 1.1 drops, and the equation is simplified as shown in Eq. 1.7.

$$\mu \nabla^2 u = \rho \frac{\partial^2 u}{\partial t^2} \tag{1.7}$$

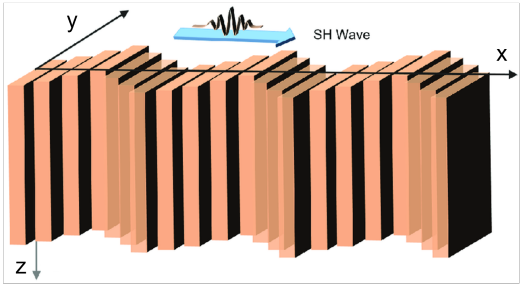

Figure 1.1: Schematic of shear horizontal (SH) wave propagation [10]

A solution to this equation of motion is given in Eq. 1.8. The first term represents a standing wave in the y-direction while the second part represents a wave propagating in the x-direction.

$$u_z(x, y, t) = h(y) e^{i(\xi x - \omega t)} \tag{1.8}$$

The characteristic equation given in Eq.1.10 is then obtained by imposing traction free boundary conditions as in shown in Eq. 1.9.

$$\sigma_{yz}(x, y, t)|_{y=-d} = 0 \tag{1.9}$$

$$sin(\eta d) cos(\eta d) = 0 \tag{1.10}$$

SH waves can be symmetric or anti-symmetric. The values of $sin(\eta d) = 0$ lead to the symmetric modes (S-modes) while the solutions of $cos(\eta d) = 0$ to the anti-symmetric ones (A-modes).

Lamb Waves

Lamb waves are vertically polarized, and they are categorized as symmetric or longitudinal (S0, S1, S2,...) and antisymmetric or flexural waves (A0, A1, A2,...).

The first anti-symmetric wave mode A_0 can be considered similar to a bending or flexural wave, with large out-of-plane displacement and smaller, anti-symmetric in-plane motion. The first symmetric

Lamb mode S_0 resembles a longitudinal wave with large, symmetric in-plane displacement. The first longitudinal (symmetric) and flexural (antisymmetric) wave mode are shown in Figure 1.2, it is also worth mentioning that in isotropic materials Lamb wave fronts propagate in circular pattern as opposed to anisotropic ones (e.g. composites).

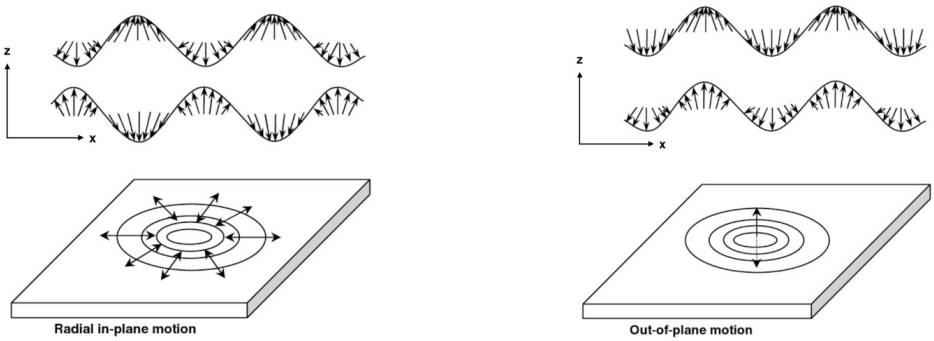

Figure 1.2: Symmetric (left) and antisymmetric (right) Lamb wave modes [11]

Harmonic solutions of the following form satisfy Eq. 1.4 and Eq. 1.5

$$f(y) = A_1 \sin(\eta_P y) + A_2 \cos(\eta_P y) \tag{1.11}$$

$$h(y) = B_1 \sin(\eta_s y) + B_2 \cos(\eta_S y) \tag{1.12}$$

The coefficients A_1, A_2, B_1, B_2 are found by the boundary conditions in Eq. 1.13.

$$\sigma_{yy}\big|_{y=\pm d} = 0, \quad \sigma_{xy}\big|_{y=\pm d} = 0 \tag{1.13}$$

where, $\eta_P = \sqrt{\frac{\omega^2}{c_P^2} - \xi^2}$ and $\eta_S = \sqrt{\frac{\omega^2}{c_S^2} - \xi^2}$

First σ_{yy} and σ_{xy} are expressed in terms of the potentials Φ and H and then in terms of functions $f(y)$ and $h(y)$. Finally, the boundary conditions are imposed. A system of four homogeneous algebraic equations is then derived, however this system can be reduced to a couple of 2 x 2 systems one for symmetric and one for antisymmetric motion.

The solution of the said systems is obtained if the determinant is zero. Thus the following equations are derived for symmetric modes Eq. 1.14 and antisymmetric ones Eq. 1.15. These equations are referred in the literature as Rayleigh-Lamb equations. The steps for their derivation can be found in Giurgiutiu [9].

$$\frac{\tan \eta_P d}{\tan \eta_S d} = -\frac{\left(\xi^2 - \eta_S^2\right)^2}{4\xi^2 \eta_P \eta_S} \tag{1.14}$$

$$\frac{\tan \eta_p d}{\tan \eta_S d} = -\frac{4\xi^2 \eta_P \eta_S}{\left(\xi^2 - \eta_S^2\right)^2} \tag{1.15}$$

Solution of Eq. 1.14 yields the symmetric eigenvalues $\xi_0^S, \xi_1^S, \xi_2^S, \ldots$ which are also the wave numbers of the symmetric Lamb waves. The relation $c = \omega/\xi$ leads to the dispersive wave speed, which is a function of the thickness frequency product fd. The same holds for the solution of Eq. 1.15. Note, that although the roots of these equations can be complex, attention is given to real and imaginary roots that correspond to propagating waves and evanescent waves respectively.

Dispersion curves
A dispersive medium causes different frequency components of a wave packet to travel at different velocities, altering the shape of the wave over time and distance.

Phase velocity c_p is the speed with which each phase propagates in space while group speed c_g is the speed at which the wave packet travels. Group speed is also used to determine how fast the energy propagates in the structure.

Phase speed and group speed are related according to Eq. 1.16.

$$c_g = \frac{d\omega}{dk} = c_p + k\frac{dc_p}{dk} \tag{1.16}$$

Regarding GUW in plates, all the modes except for the fundamental shear horizontal (SH0) are dispersive, meaning that the initial shape of the wave signal changes with time and distance.

Figure 1.3 displays the phase and group velocity dispersion curves of Lamb waves in an aluminum plate. By observing these curves one can notice that at low frequency thickness product only the two fundamental modes propagate. For increasing thickness-frequency product multiple wave modes can propagate, above the cut-off frequencies of the higher wave modes. At the cut-off frequencies the group velocity of the specific wave mode tends towards zero, while its phase velocity tends towards infinity.

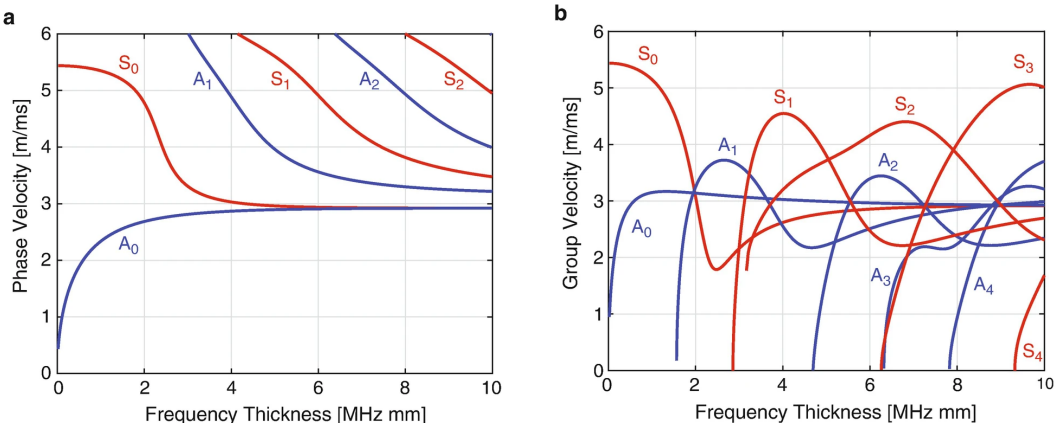

Figure 1.3: Dispersion curves for aluminum plate; (a) Phase velocity and (b) group velocity [7]

1.4. Ultrasonic waves in NDT and SHM

1.4.1. From Bulk waves to Guided Waves

Traditional ultrasonic NDT techniques rely on bulk waves, which are ultrasonic waves with wavelengths shorter than the thickness of the specimen under inspection. These waves propagate in the through thickness direction.

On the other hand, GUW have wavelengths larger than the thickness of the material and travel along the specimen. Figure 1.4 illustrates how bulk and ultrasonic waves propagate in a thin-walled structure with a defect, in the context of active ultrasonic testing.

SHM with GUW is based on the recording and post-processing of the transient stress waves emitted from the sudden release of energy due to impacts or damage initiation and growth in the material. The technique has already proven to be a valuable option for the integrity assessment of various structures such as steel bridges [2, 12, 4], large offshore structures [5, 3, 6] and pipelines [7, 13].

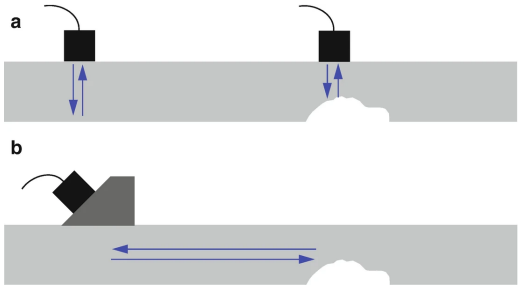

Figure 1.4: Schematic of (a) bulk and (b) guided ultrasonic wave testing [7]

1.4.2. Fundamentals of GUW based SHM

GUW based SHM systems can be divided in two categories active and passive, as shown in Figure 1.5. An active SHM system consists of actuators and sensors. More specifically, an actuator generates a source wave in the structure. GUW propagate in the material and interact with the boundaries and defects. The response at various locations is then recorded and processed to identify the damage.

On the other hand, a passive SHM system continuously obtains measurements from suitable sensors installed on the structure. AE are generated by damage or external impacts. The response is first recorded at different locations, then is post-processed to identify possible damage or the impact's location and severity.

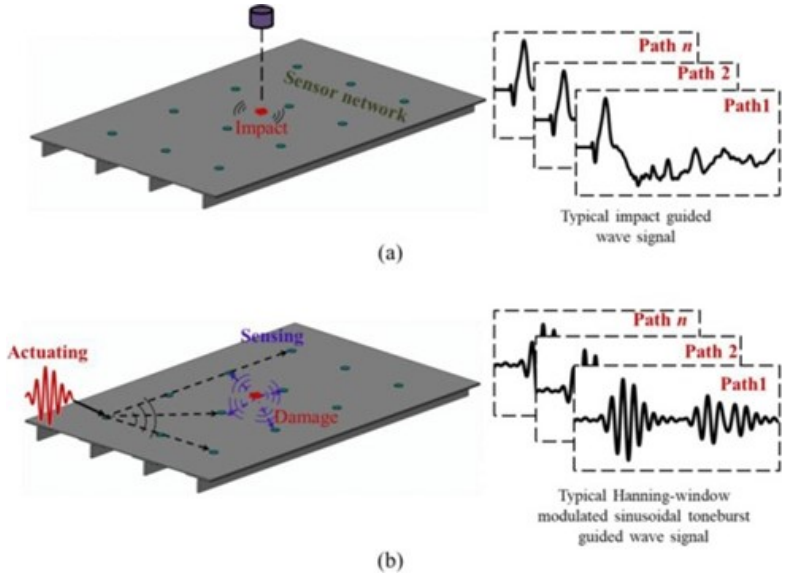

Figure 1.5: (a) Passive and (b) Active guided ultrasonic wave SHM [14]

During impacts, a part of the energy travels the structure as guided waves. As a result, GUW are suitable for SHM in this kind of applications. In the following section the existing literature on impact identification is be discussed.

1.5. Literature review on impact localization

Impact source localization is typically considered an inverse problem. GUW emitted during an impact are captured by the sensors and then, they are processed to identify the source location.

This chapter reviews guided wave based methods for impact source localization focusing on their application in thin-walled structures such as plates and stiffened panels which are representative of ship structures.

First, the state-of-the-art on impact localization in plates and stiffened panels is presented. Subsequently,

although not directly connected to impact localization, research findings on the transmission coefficient of GUW through stiffeners are outlined. These structural discontinuities affect wave propagation and attenuate wave the signals, potentially reducing detectability by the sensors. The transmission coefficient quantifies the fraction of wave energy that successfully passes through the stiffener, providing insight into how structural discontinuities affect wave propagation.

1.5.1. State-of-the-art for impact identification

Relevant impact localization methods include:

- Time Difference Method
- Impulse Response Function (IRF) Database Method
- Virtual Time Reversal (TR)
- Machine Learning Methods

Time difference method

One popular impact localization strategy is based on the time of flight (ToF) of transducers. To pinpoint the emission source, usually an array of sensors is used. By calculating the time of arrival differences for each pair of sensors, two hyperbolae are formed. The intersection of these hyperbolae provides the location of the emission source [15]. Ciampa and Meo [16] employed Continuous Wavelet Transform (CWT) to determine the time of flight (ToF) of each sensor to locate the impact location by solving a non-linear equation of wave velocity and impact coordinates. Migot and Giurgiutiu [17] developed a source localization methodology employing triangulation technique, which is illustrated in Fig. 1.6, which does not require the wave velocity for the calculation of ToF. The ToF is calculated through the CWT. The number of required sensors was investigated by conducting experiments where a small steel ball impacted an aluminum plate. They concluded that the accuracy increases with increased number of transducers. AE source localization methods based on the Time Distance Domain Transform (TDDT) [18] have been proposed in the literature [19, 20]. The unknown time delay between the AE event and the recording is determined by finding the most compressed distance transformed signal after dispersion compensation. This enables the estimation of source to sensor distances for the individual transducers which can be then combined for source localization through triangulation.

Although the principle of Time Difference Method is straightforward its accuracy depends on the measured ToF which is vulnerable to the environmental conditions such as noise and thickness changes. Furthermore, stiffeners, rivets and other geometrical irregularities hinder its precise identification making the method unsuitable for structures such as stiffened panels [21, 22].

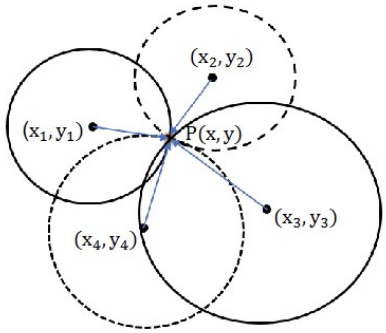

Figure 1.6: Triangulation of four transducers for impact localization [17]

Impulse Response Function (IRF) Database Method

Ing et al. [23] proposed another impact localization algorithm for the detection of a finger knock on a glass plate. This method involves collecting an IRF data set by mechanically impacting multiple points within a target structure and measuring the corresponding IRFs at a surface-mounted sensors. The actual impact source is located by identifying which IRF in the data set gives the maximum correlation

with the IRF generated by the actual impact. The correlation operation is mathematically equivalent of the convolution between the one IRF and the time reversed version of the other [24]. According to the Time Reversal (TR) focusing property the correlation is maximized when the training point and the actual impact point match. This method is very powerful because it does not require the knowledge of the wave velocity or the structural geometry [24]. Therefore, it effectively addresses challenges associated with GUW propagation in complex structures such as dispersion, scattering, and mode conversion. Regarding impact localization in plates, Ciampa and Meo [25] presented a method for real-time localization of impact sources in complex composite structures. The said IRFs were obtained experimentally by systematically exciting the structure at predefined observation points and recording the resulting waveforms utilizing a single passive sensor. Experimental validation on a stiffened composite panel demonstrated high localization accuracy, with a maximum error of less than 3%. Park et al. [24] automated and expedited the database creation process by using a Scanning Laser Doppler Vibrometer (SLDV). The effectiveness and robustness of this approach were proven by experiments on a composite aircraft wing and an aluminum fuselage section, despite the complexity of the structures. Concerning the applicability and practicality of this method in real world applications, the challenge to overcome is the long lasting repeated process of impacts to obtain the IRF database. Miniaci et al. [22] showed that the impact location can be identified by using only one piezoelectric transducer, their approach is based on the methodology proposed by Park et al. [24]. They performed numerical FE simulations and experimental measurements on an eccentrically stiffened aluminum panel to prove the suggested procedure.

Virtual TR

Another method for impact source localization is based on virtual TR. This approach involves two key steps. First, the response of an impact is recorded by an array of transducers placed on the structure. In the second step, the recorded signals are time-reversed and re-emitted by each transducer. The second step is performed in a virtual environment hence the term "virtual". Taking advantage of the spatial and temporal focusing properties of time reversed guided waves, the emitted waves converge at the original impact location, enabling source localization. Pahlavan [26] validated the concept of passive TR in laboratory experiments, by exciting waves on graphite-epoxy plate with an actuator. The practical feasibility of virtual TR for SHM applicationswas proven since the AE source was localized with an error of 6.7%. The backward propagation of the recorded waves was performed with a 2D wavelet-based spectral finite element method. The only work focusing on impact localization in stiffened panels using a time reversal concept is published by Yu et al. [27]. Numerical and experimental studies were carried out on an aluminum stiffened panel, the acoustic emission source was created by Pencil Lead Break (PLB) tests. In their work a novel numerical simulation technique is proposed to deal with the possible defocus of the re-emitted signal due to signal reflection and scattering from the stiffeners. Time domain spectral finite element method is utilized to simulate the back propagating wave field. Following this research Yu et al. [21] published a paper on impact localization and impact force reconstruction on composite plates. They used the spatial and temporal focusing properties of time reversal to locate the impact source and restore the impact force. The proposed methodology was also validated experimentally, the impacts involved a metallic ball falling freely on the monitored plate.

Machine Learning Methods

Machine learning (ML) has been also implemented in impact localization, offering adaptability and scalability. Among the ML techniques, the most prominent are Artificial Neural Networks (ANNs) and Support Vector Machines (SVMs). Ghajari, Khodaei, and Aliabadi [28] applied ANNs trained with FE data for impact localization in stiffened panels. The study notes the high cost of experimental data acquisition. Hossain et al. [29] improved localization precision by fusing accelerometers and radial basis function networks (RBFN). Yang et al. [14] in their review paper noted that ANN performance rely heavily on large training data sets which in most cases are very difficult to collect. Support Vector Machines were therefore proposed as an alternative since they require less data and are hence more economical for SHM. Yang and Xu [30] proposed a deep learning approach by utilizing Stacked Denoising Autoencoders (SDAE) and reported a higher localization accuracy than the traditional techniques. The environmental variables such as temperature and vibrations, are still a challenge to these techniques.

Summary
Impact localization methodologies have evolved significantly. Straightforward techniques that measure the signals' Time of Flight (ToF) and employ a geometrical approach to identify the location such as triangulation offer simplicity but face limitations in complex structures. TR approaches have emerged as a promising solution, leveraging guided waves spatial reciprocity and time reversibility to overcome challenges such as dispersion and scattering. Ciampa and Meo [16], Pahlavan [26], and Yu et al. [27, 21], have experimentally demonstrated the practical feasibility and accuracy of TR based methods in complex structures like composite plates and stiffened panels. Machine learning algorithms provide adaptability and scalability, though challenges related to large training datasets and environmental factors persist.

1.5.2. Propagation of guided waves in stiffened panels

Several studies have been published concerning the propagation characteristics of GUW in stiffened panels, focusing on phenomena such as reflection, transmission and mode conversion of waves due the presence of structural discontinuities such as stiffeners [31, 32]. The methodology presented in Chapter 2, makes use of the Transmission Coefficient (T_c) therefore only literature relevant to this is presented. The TC is used to quantify the wave energy that propagates through the stiffener. According to Han et al. [31], it is the ratio of signal amplitudes at a predefined location, with the numerator being the signal amplitude when a stiffener is present and the denominator the amplitude when it is not. Saccone and Pahlavan [33] define it as the ratio of signal amplitude before and after the stiffener. Given the minimal energy loss of guided waves in a plate, these expressions can be considered equivalent.

Han et al. [31] calculated the T_c both numerically and experimentally for various frequencies and stiffener heights in an aluminum plate. The results show good agreement. Their experimental set-up involved an aluminum plate and an aluminum stiffened panel, the plates had the same dimensions (300x600 mm^2) and 5 mm thickness and the stiffener height was 7 mm. The results show that the transmission coefficient for mode $A0$ ranges between 0.50 and 0.72, showing an initial increase, reaching a peak and then decreasing with a constant slope for increasing central excitation frequency ranging from 100 to 170 kHz. Saccone and Pahlavan [33] studied the transmission of GUW and their dependence on the angle of incidence on a stiffener. The estimation of the T_c was carried out by combining experimental results and numerical simulations. The AE signals were generated by PLBs. The transmission coefficient was calculated for a steel stiffened panel ranging between 0.65 and 0.55 for different angles of incidence. The sensors used in the experiments have the capability to capture signals between 100 and 200 kHz. Wang et al. [34] developed a 2D Fast Fourier Transform (FFT) method to analyze the transmission characteristics in aluminum stiffened panels with I-type and L-type stiffeners. The results showed that the for the same size stiffener the transmission coefficient for Lamb waves varied for wave frequencies, ranging from 50 to 500 kHz. The transmission coefficient was validated both through numerical simulations carried out in ABAQUS and with experimental measurements. The transmission coefficient was extremely small in a certain frequency range and showed no constant behavior, but considerable fluctuations ranging from 0.15 to 0.90.

Based on the Figures 1.7 and 1.8 presented below, the TC fluctuates with frequency. The present study focuses on waves with frequencies between 20 and 100 kHz, therefore following the results of Han et al. [31] and Saccone and Pahlavan [33] a T_c equal to 0.65 is assumed.

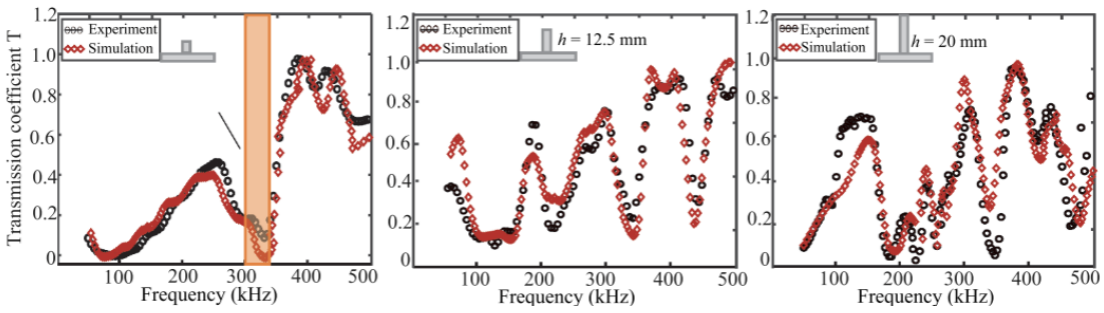

Figure 1.7: Transmission coefficient in aluminum stiffened panels with various stiffener heights [34]

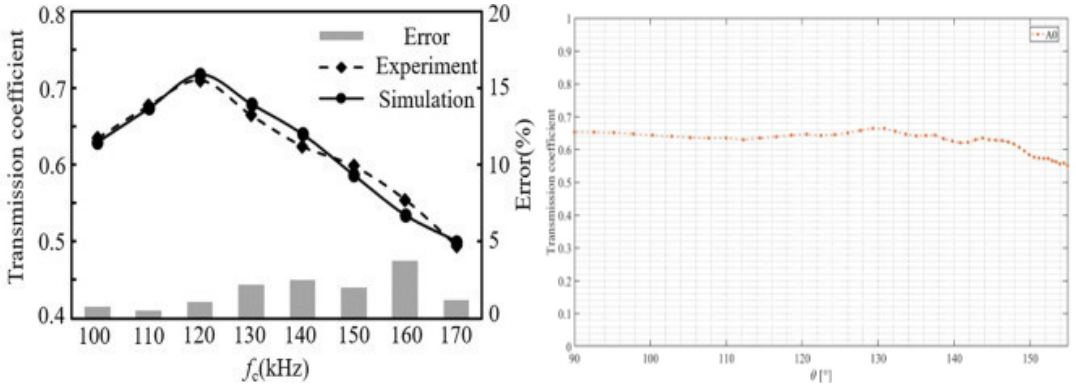

Figure 1.8: Transmission coefficient; Han et al. [31] (left); Saccone and Pahlavan [33] (right)

1.6. Objective

1.6.1. Knowledge gap

The literature review suggests that impact localization in stiffened panels has not been fully explored.

The straightforward and intuitive impact source localization methods are based on the signals' ToF. However, accurate determination of the ToF is difficult due to the existence of noise in the recorded signals [35]. Identifying the ToF in noisy environments and complex structures with features like stiffeners which introduce wave reflections, scattering and mode conversions and associating it with the correct propagating mode is even more complicated.

Data driven methods, such as the IRF database techniques, have proven to be effective and powerful, also for complex composite structures [24]. The main advantage is that there is no knowledge requirement for the wave velocity and the structure's properties. However, these methods require structure specific IRF databases. The latter are acquired through numerous impact tests, a process not feasible for large-scale structures such as ships. Similarly, ML techniques, while adaptable, are computationally expensive due to the need for large datasets and are sensitive to environmental parameters such as vibrations.

Impact localization is an inverse problem, and involves determining the impact location (input) based on measured sensor data (response). Inverse problems are usually ill-posed, by either lacking unique solutions or by being unstable [36, 35]. The former issue arises because the sensors cannot capture all the information released during the impact and the latter because small sensor perturbations result in large deviations when determining the impact source.

Pahlavan [26] proposed a source localization using the virtual TR of ultrasonic wave fields, transforming the ill-conditioned inverse problem into a forward problem. This approach exploits the inherent properties of time reversibility and spatial reciprocity of elastic wavefields which allow to pinpoint the excitation source in various media. The practicality and the effectiveness of this approach has been demonstrated in composite plates [26, 21] and small aluminum stiffened panels [27], as discussed in Chapter 1.5. The capability to overcome the aforementioned traditional method limitations establishes virtual TR as a promising technique for impact localization, however its application on representative ship structures and impacts remains limited.

1.6.2. Research Objective and Research Questions

The objective of this project is to evaluate and demonstrate the feasibility of impact localization on steel stiffened panels, representative of ship hulls structures, by monitoring AE generated by impact events and applying virtual time reversal techniques at both small and large scale.

Based on this objective and the findings of this thesis, the following main research question is formulated:

Can virtual TR of GUW be effectively used to localize impact sources in steel stiffened panels, both at laboratory and full scale?

To address the main research question, several key sub-questions are formulated to tackle different aspects of the problem.

- **RQ1:** Which guided wave modes are expected to dominate the recorded signals in steel plates and stiffened panels under impact testing?
  - *Hypothesis:* The fundamental symmetric (S0) and antisymmetric (A0) wave modes are expected to propagate given the thickness of the specimens and the frequency content excited by the impact. The use of surface-mounted piezoelectric sensors with magnetic holders makes them primarily sensitive to out-of-plane deflection, therefore A0 wave mode is likely to dominate the recorded signals.
- **RQ2:** How can structural features such as stiffeners be approximated within the virtual time reversal framework to maintain localization accuracy?
  - *Hypothesis:* The presence of stiffeners can be reasonably modeled using a scalar transmission coefficient T_c, applied as an attenuation factor.
- **RQ3:** How does localization performance change when transitioning from small-scale laboratory setups to full-scale ship structures, and what factors contribute most to this degradation?
  - *Hypothesis:* While full-scale application introduces additional propagation paths acceptable localization accuracy can still be achieved with appropriate sensor type and array configuration.

1.6.3. Novelty

The present research builds upon the concept of virtual TR for AE source localization, as discussed in Pahlavan [26]. An analytical formulation, suitable for practical applications, that describes the wave propagation in the monitored area is utilized. The key novelty lies in extending the TR framework from plates to stiffened plates and panels by incorporating the effect of stiffeners during back propagation. This is achieved by considering the research findings of Saccone and Pahlavan [33], who quantified the transmission characteristics of GUW across stiffeners, and introducing a transmission coefficient T_c in the analytical model.

This adjustment enables the use of virtual TR for source localization in complex structures such as stiffened panels which are representative of large structures such as ships and bridges. Additionally, unlike existing research which often relies on actuators to generate GUW signals, the present work deals with the complexities of realistic impact events by employing PLBs and instrumented hammer hits as AE sources. The proposed methodology for source localization is validated on both laboratory specimens and a full scale ship structure, demonstrating its applicability across different scales.

2

Methodology

2.1. Overview

This chapter discusses the impact identification methodology developed to address the main research question of the previous chapter. The methodology consists of two main components, an experimental and an analytical. In the experimental stage, controlled impacts are performed on test structures and the AE generated during the impact are recorded using piezoelectric (PZT) sensors. In the subsequent analytical stage, the collected data is processed and the wavefield at the time of the impact is reconstructed in a virtual environment using TR. The methodology framework is shown in Figure 2.1.

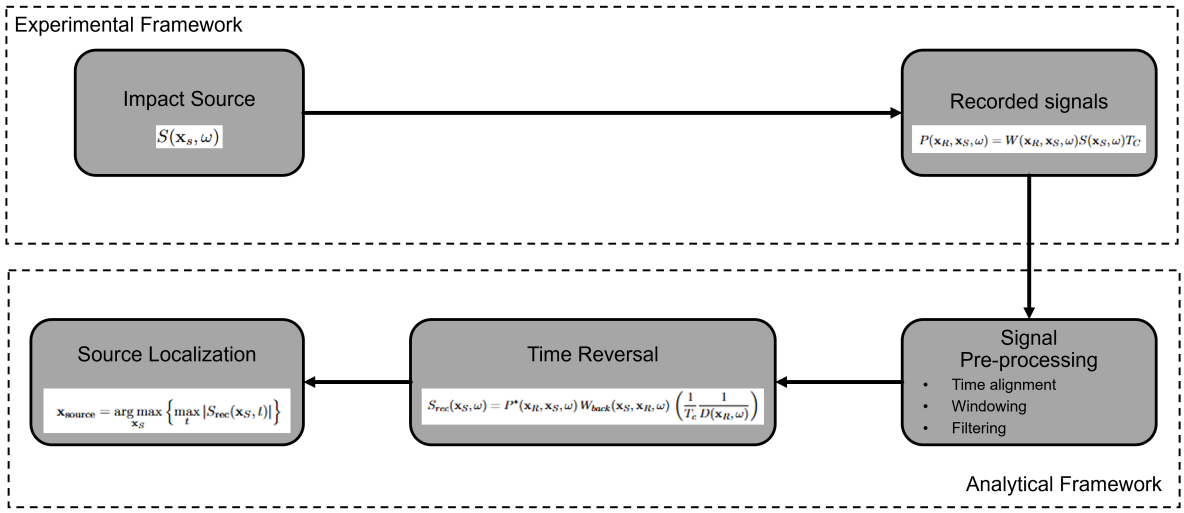

Figure 2.1: Impact localization approach.

2.2. Experimental Framework

The experiments are carried out in two phases. Small scale laboratory experiments are performed in the Structures Laboratory of TU Delft, and large scale experiments are performed onboard a Shoalbuster under construction at Damen Shipyards in Gorinchem.

The lab tests serve as a feasibility study, validating the proposed monitoring and localization methodology under controlled conditions. The full-scale experiments are an attempt to extend the approach to more realistic and complex geometries, allowing the evaluation and the scalability and the robustness of the method.

In both campaigns, controlled impacts were performed at known locations, and the resulting guided

wave signals were recorded using surface-mounted piezoelectric sensors. These signals serve as the input to the localization algorithm described in the following sections.

Two types of AE sources were used, Pencil Lead Breaks (PLBs) and an instrumented hammer. The PLBs produce short pulses, with the frequency content spread among a wide frequency range while the instrumented hammer generates longer-duration signals that last several milliseconds, and most of their energy is concentrated in lower frequencies.

Further details on the experimental setups and instrumentation are provided in Chapters 3.1 and 3.2.

The signals recorded during the experiments are prepared for analysis through pre-processing, which involves synchronizing signal arrival times, isolating the dominant propagating mode and removing noise. These steps are detailed in Chapter 4.

2.3. Analytical Framework

The analytical framework consists of back-propagating the recorded signals in time in order to focus on the emission location according to the TR properties. First, the theoretical foundation of the TR property is briefly presented before discussing its implementation.

2.3.1. TR - Theoretical Background

TR was introduced by Fink [37] in the framework of acoustic wave propagation in inhomogeneous media, within the range of sonic and ultrasonic frequencies assuming that the process is adiabatic. Time reversal relies on two key principles of wave equations time reversibility and spatial reciprocity, which allow recorded signals to be reversed in time and back-propagated, focusing on their origin

The wave equation of an acoustic pressure field $p(r,t)$ is given below, where, $\rho(r)$ is the density that varies with space and c the local sound velocity.

$$\nabla \cdot \left(\frac{\nabla p}{\rho} \right) - \frac{1}{\rho c^2} \frac{\partial^2 p}{\partial t^2} = 0 \tag{2.1}$$

According to time reversibility if $p(x,t)$ is a solution, then $p(x,-t)$ is also a solution. This enables the waveforms to be reversed in time and re-propagated back to the source. Spatial reciprocity is the property according to which only the relative positions of the source and the receiver matter. Thus, their interchange is enabled which ensures that time reversed waves retrace their original paths.

The TR process for source localization as described by Fink [37] is shown in Fig 2.2 and involves two steps. In the first step, an emission from a point source propagates through an inhomogeneous medium which contains a cavity, and is recorded by an array of receivers. In the second step, each transducer emits the time reversed recorded signal. Thanks to the time reversibility and spatial reciprocity properties, discussed above, the time-reversed waves converge at the original source location achieving spatial and temporal focusing. This focusing allows the localization of the emission source.

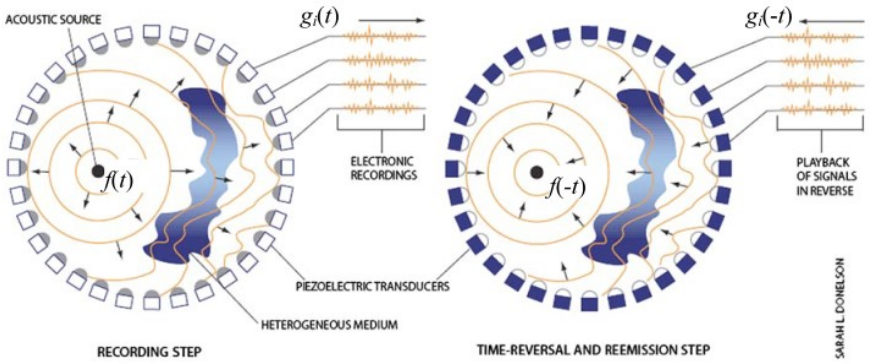

Figure 2.2: Time reversal procedure using a Time Reversal mirror [38]

The key takeaway of TR is that for a point-like source, it allows spatial focusing back to the original source regardless of the medium complexity [38]. This is achieved by using TR mirrors, a practical implementation of Phase Conjugate Mirrors (PCM) [39]. A PCM unlike an ordinary mirror, which does not change the time ordering of events, flips the chronological order of events as shown in Figure 2.3.

A TR Mirror extends this idea by using an array of transducers that record the incoming wave signals, reverse them in time, and finally re-emit them. This process reproduces the phase conjugation effect of PCM but in a system with multiple sensors.

Equation 2.2 denotes the Fourier transform of the recorded pressure signal $p(x,t)$.

$$p(x,\omega) = \int_{-\infty}^{\infty} p(x,t)e^{-i\omega t}dt \tag{2.2}$$

Then, the time reversed signal, $p(x,-t)$ is transformed in the frequency domain according to Equation 2.3.

$$p(x,-\omega) = \int_{-\infty}^{\infty} p(x,-t)e^{-i\omega t}dt = p^*(x,\omega) \tag{2.3}$$

The equality $p(x,-\omega) = p^*(x,\omega)$ follows from the Hermitian symmetry of real valued signals. Thus in the frequency domain time reversal reduces to taking the complex conjugate of the recorded spectrum.

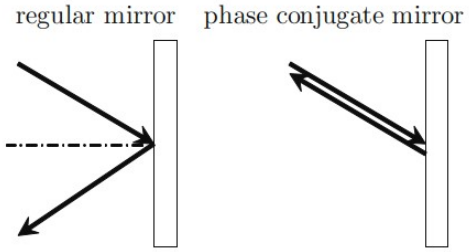

Figure 2.3: Regular mirror vs Phase Conjugate Mirror (PCM) [26]

2.3.2. Propagation of Guided Ultrasonic Waves

In thin-walled structures such as plates and stiffened panels AE signals propagate as GUW. In this work, wave propagation is modeled in the frequency domain to simplify the treatment of dispersion, attenuation, and time reversal operations. The modeling approach begins with plates and is then extended to stiffened panels.

The recorded time-domain signals are transformed into the frequency domain using the Fourier transform:

$$P(\omega) = \int_{-\infty}^{\infty} P(t)\, e^{-i\omega t}\, dt \tag{2.4}$$

where, $P(t)$ denotes the time domain signal recorded at a given sensor, and $P(\omega)$ its frequency domain representation.

Wave propagation in plates

Consider an impact at an arbitrary point on a steel plate, as shown in Figure 2.4. The impact location is denoted by the star, the half sinusoidal signal is representative of an impact pulse and the recorded signal at the sensor is the result of the convolution terms described in Equation 2.5.

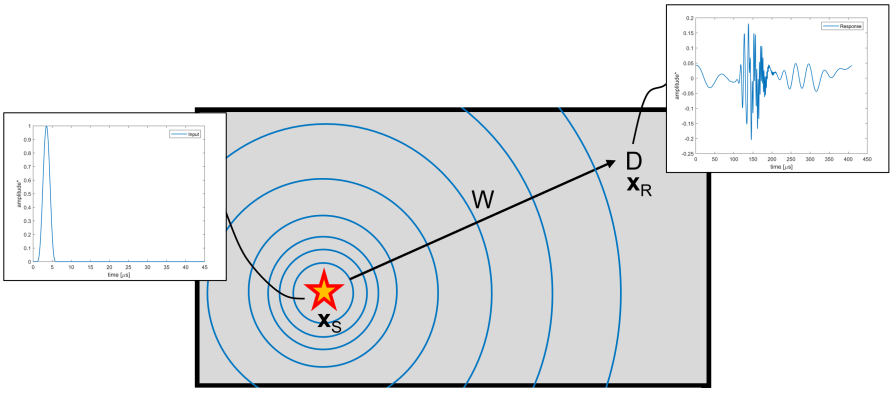

Figure 2.4: Elastic wave propagation in a steel plate

Equation 2.5, describes the multi-modal propagation of guided waves in the frequency domain as the superposition of the i propagating modes. The source signal $S(\mathbf{x}_s, \omega)$, is convolved with the sensor's electromechanical transfer function $D_i(\mathbf{x}_R, \omega)$ and with the medium transfer function $W_i(\mathbf{x}_R, \mathbf{x}_S, \omega)$. The notation and the properties of the operators are detailed in Berkhout [40].

$$P(\mathbf{x}_R, \mathbf{x}_S, \omega) = \sum_{i=1}^{n} D_i(\mathbf{x}_R, \omega) W_i(\mathbf{x}_R, \mathbf{x}_S, \omega) S(\mathbf{x}_S, \omega) + P_N(\mathbf{x}_R, \omega) \tag{2.5}$$

with,
$P(\mathbf{x}_R, \mathbf{x}_S, \omega)$ the response recorded by the receiver,
$S(\mathbf{x}_s, \omega)$ the AE source signal,
$D_i(\mathbf{x}_R, \omega)$ the transfer function of the receiver for the mode i,
$W_i(\mathbf{x}_R, \mathbf{x}_S, \omega)$ the medium transfer function for mode i between the source and the receiver,
$P_N(\mathbf{x}_R, \omega)$ the measurement noise,
$\mathbf{x}_S$ the location of the source,
$\mathbf{x}_R$ the location of the receiver,
i being the guided wave modes S0,S1,S2,...,A0,A1,A2,
ω being the angular frequency.

In this study only the fundamental anti-symmetric mode A0 is used for source localization. This choice is supported by preliminary tests which confirmed that the PZT sensors utilized are more sensitive to the out-of-plane motion, as shown in Appendix B. Assuming single mode mode transmission and that the noise is adequately filtered out, Equation 2.5 is reduced to the following form.

$$P(\mathbf{x}_R, \mathbf{x}_S, \omega) = D(\mathbf{x}_R, \omega) W(\mathbf{x}_R, \mathbf{x}_S, \omega) S(\mathbf{x}_S, \omega) \tag{2.6}$$

Furthermore if the coupling variation between each sensor and the structure is small and the sensor response is flat across the frequency range of interest, the electromechanical transfer function of the sensors $D(\mathbf{x}_R, \omega)$ is approximated by unity across the entire frequency range and can be also dropped from the equation [41], resulting in Equation 2.7.

$$P(\mathbf{x}_R, \mathbf{x}_S, \omega) = W(\mathbf{x}_R, \mathbf{x}_S, \omega) S(\mathbf{x}_S, \omega) \tag{2.7}$$

Medium Transfer function

The medium transfer function $W_i(\mathbf{x}_R, \mathbf{x}_S, \omega)$ describes how the signal propagates from the source to the receiver through the structure. It includes dispersion by using frequency dependent phase velocity and amplitude decay due to geometric spreading. The medium transfer function is decomposed into two parts:

- A phase term, capturing the dispersive propagation of guided waves
- An amplitude scaling term representing amplitude decay with distance

Phase term
The phase delay for a wave traveling distance $d = |\mathbf{x}_R - \mathbf{x}_S|$ is modeled by a frequency-dependent exponential term [42, 18]. This term ensures that each frequency component experiences the appropriate phase shift during wave propagation. The general expression is shown in Equation 2.8. The steps to obtain the phase term are presented in Appendix A.

$$W_i(\mathbf{x}_R, \mathbf{x}_S, \omega) = exp\left(\frac{-i\omega d}{c_p^{(i)}(\omega)}\right) \tag{2.8}$$

where, $c_p^{(i)}(\omega)$ is the frequency dependent phase velocity of the propagating mode

This formulation can be extended to plates with non uniform thickness. Consider a plate of two segments with thicknesses t_1 and t_2 corresponding to phase velocities $c_p^{(1)}(\omega)$ and $c_p^{(2)}(\omega)$ respectively. If d_1 and d_2 are the distances traveled by the wave in each segment of the plate the total phase delay becomes the product of the individual phase delays as shown in Equation 2.9.

$$W_i(\mathbf{x}_R, \mathbf{x}_S, \omega) = exp\left(\frac{-i\omega d_1}{c_p^{(1)}(\omega)}\right) exp\left(\frac{-i\omega d_2}{c_p^{(2)}(\omega)}\right) \tag{2.9}$$

Amplitude Scaling term
Signal amplitude decay is the result of material damping and geometric spreading. In this work material damping is considered negligible.

To account for geometric spreading, the amplitude decay is modeled by assuming cylindrical wave expansion. As the wavefront expands, the wave's amplitude should decreases to keep constant energy at each radius and not violate energy conservation. The expression for the scaling factor $\alpha(\mathbf{x}_R, \mathbf{x}_S, \omega)$ is shown in Equation 2.10.

$$\alpha(\mathbf{x}_R, \mathbf{x}_S) = \sqrt{\frac{L_{ref}}{|\mathbf{x}_R - \mathbf{x}_S|}} \tag{2.10}$$

where, L_{ref} is a reference length, here taken as the radius of the piezoelectric sensor.

Complete Expression
Combining the two terms described above, the complete expression of the medium transfer function for a single wave mode propagating across distance $d = |\mathbf{x}_R - \mathbf{x}_S|$ is obtained according to Equation 2.11.

$$W(\mathbf{x}_R, \mathbf{x}_S, \omega) = exp\left(\frac{-i\omega d}{c_p(\omega)}\right)\sqrt{\frac{L_{ref}}{d}} \tag{2.11}$$

This function models how the wave propagates and how its amplitude decays over distance.

2.3.3. Propagation in Stiffened Panels

Ship hull structures are composed of stiffened panels, thus the presence of the stiffeners should be considered in the propagation model.

In a simplified representation, it is assumed that the wave traveling directly from the source ($\mathbf{x}_S$) to the receiver ($\mathbf{x}_R$) encounters a stiffener, resulting in partial reflection and transmission of wave energy. In the present thesis reflections are not modeled, and the attenuation is described by introducing the stiffener transmission coefficient $T_c(x_{st}, \omega)$.

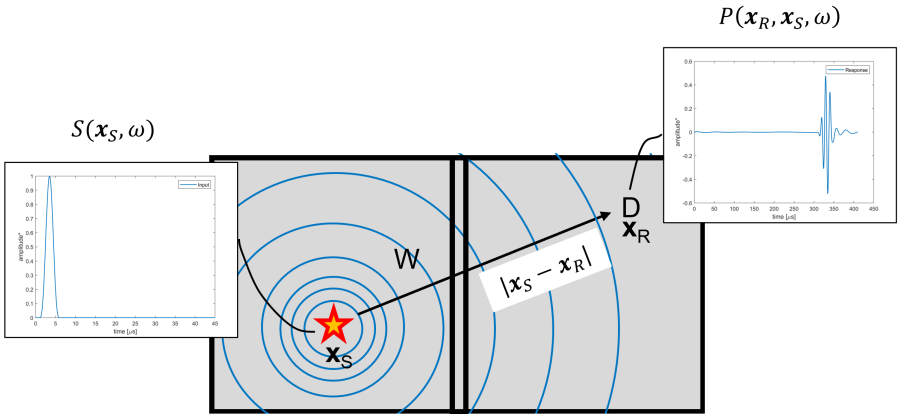

Figure 2.5: Elastic wave propagation in a steel stiffened panel

Following Saccone and Pahlavan [33], the transmission coefficient T_c across a stiffener can be approximated as $T_c \approx 0.65$ for angles of incidence between 90° and 150°, although a slight reduction is seen at larger angles. Assuming angle and frequency independence in the range or interest $T_c(x_s, \omega)$ can be simplified and be treated as a scalar T_c [41].

Therefore, GUW propagation in a stiffened plate is described by Equation 2.12

$$P(\mathbf{x}_R, \mathbf{x}_S, \omega) = T_c W(\mathbf{x}_R, \mathbf{x}_S, \omega) S(\mathbf{x}_S, \omega) \tag{2.12}$$

In actual ship structures the waves interact with multiple stiffeners. Assuming that each stiffener contributes independently and that the same transmission coefficient applies to each interaction, the cumulative effect of N stiffeners is condensed into a single scalar attenuation factor raised to the power of the number of stiffeners intersected, as shown in Equation 2.13.

$$P(\mathbf{x}_R, \mathbf{x}_S, \omega) = T_c^N W(\mathbf{x}_R, \mathbf{x}_S, \omega) S(\mathbf{x}_S, \omega) \tag{2.13}$$

2.3.4. Time Reversal - Source localization

In this chapter the general case of a stiffened plate is considered; in the case of a plate, no stiffener attenuation occurs and the scalar T_c is replaced by unity.

To reconstruct the wavefield at distance d from the recording location, the recorded signal is time-reversed and emitted from the receiver locations. Because the process takes place in the frequency domain signal time reversal is equivalent to the complex conjugation of the signal's spectrum, as previously discussed. Additionally, signal convolution in the time domain, becomes multiplication in the frequency domain which enables the removal of the effect of the transfer function of the sensor and the attenuation of the stiffener by multiplying with $1/D$ and $1/T_c$, respectively.

In the forward model, the amplitude decay due to geometric spreading is introduced in medium by multiplying with the function $\alpha(\mathbf{x}_R, \mathbf{x}_S)$. To correctly reconstruct the original wavefield during backpropagation, this amplitude decay must be compensated and the medium transfer function $W_{back}(\mathbf{x}_S, \mathbf{x}_R, \omega)$ is introduced. This medium transfer function has the same phase delay term as the one that describes the forward propagation because of spatial reciprocity but the inverse of amplitude decay term $\alpha(\mathbf{x}_R, \mathbf{x}_S)$ is used to compensate for the amplitude decrease, as shown in Equation 2.14.

$$W_{back}(\mathbf{x}_R, \mathbf{x}_S, \omega) = exp\left(\frac{-i\omega d}{c_p(\omega)}\right)\left(\sqrt{\frac{L_{ref}}{d}}\right)^{-1} \tag{2.14}$$

Therefore, the backpropagation of a signal recorded at location $\mathbf{x}_R$ to the source is described by Equation 2.15.

$$S_{rec}(\mathbf{x}_S, \omega) = P^*(\mathbf{x}_R, \mathbf{x}_S, \omega)\, W_{back}(\mathbf{x}_S, \mathbf{x}_R, \omega) \left(\frac{1}{T_c}\frac{1}{D(\mathbf{x}_R, \omega)}\right) \tag{2.15}$$

The process of backpropagation in the frequency domain is illustrated schematically in Figure 2.6, where the input signal, the time reversed recorded signal, and the reconstructed source are shown. Note, that the reconstructed signal is flipped to allow visual comparison with the input signal.

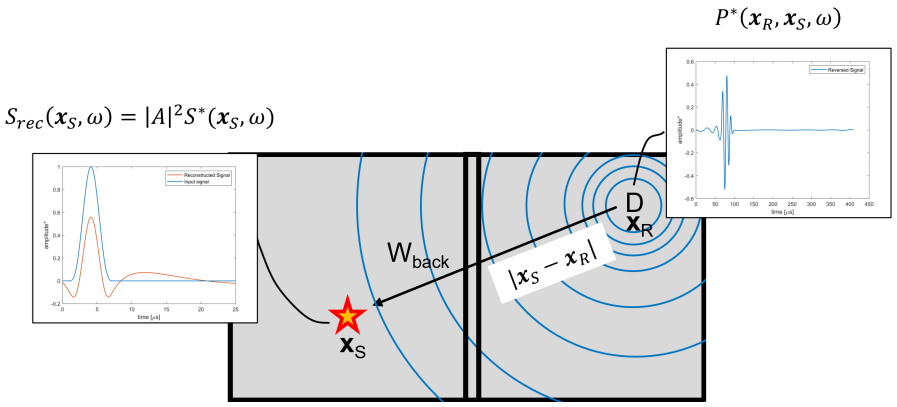

Figure 2.6: Schematic of the TR process in a stiffened plate.

where, $S_{rec}(\mathbf{x}_S, \omega)$ the reconstructed source
$P^*(\mathbf{x}_R, \mathbf{x}_S, \omega)$ the time reversed recording at the receiver location
$W_{back}(\mathbf{x}_S, \mathbf{x}_R, \omega)$ transfer function of the medium
$D(\mathbf{x}_R, \omega)$ transfer function of the receiver
T_c the transmission coefficient

By substituting P^* in Equation 2.15 with the complex conjugate expression of Equation 2.12 while considering the assumption that $D(\mathbf{x}_R, \omega)$ is unity, taking into account that spatial reciprocity holds meaning that $W(\mathbf{x}_R, \mathbf{x}_S, \omega) = W(\mathbf{x}_S, \mathbf{x}_R, \omega)$, Equation 2.16 is derived.

$$\begin{aligned} S_{rec}(\mathbf{x}_S, \omega) &= S^*(\mathbf{x}_S, \omega) \cdot W^*_{back}(\mathbf{x}_R, \mathbf{x}_S, \omega) \cdot W(\mathbf{x}_S, \mathbf{x}_R, \omega) = \\ &= S^*(\mathbf{x}_S, \omega) \cdot \exp\left(\frac{-i\omega d}{c_p(\omega)}\right) \cdot \left[\exp\left(\frac{-i\omega d}{c_p(\omega)}\right)\right]^* = |A|^2 S^*(\mathbf{x}_S, \omega) \end{aligned} \tag{2.16}$$

Equation 2.16 shows that, when the signal is backpropagated to its original source location, the result is the complex conjugate of the original source signal, scaled by the product of the forward and backward medium transfer function, since the geometric spreading and sensor transfer functions terms intentionally cancel out.

Localization Procedure with Multiple Sensors

The predicted impact location is defined as the point $\mathbf{x}_S$ on the monitored structure where the absolute maximum amplitude of the reconstructed field occurs over time.

$$\mathbf{x}_{\text{source}} = \arg\max_{\mathbf{x}_S} \left\{ \max_t |S_{\text{rec}}(\mathbf{x}_S, t)| \right\} \tag{2.17}$$

This criterion is based on the hypothesis that the back-propagated signals from multiple sensors will constructively interfere at the true source location, resulting in the largest amplitude, and destructively interfere elsewhere due to phase mismatches.

In complex structures reflected waves due to the presence of stiffeners, welds and other discontinuities are recorded by the sensors and when propagated backwards they produce multiple focal points. To

address this, the maximum amplitude of the reconstructed wavefield is used as a localization criterion. The rationale is that the point of impact generates the strongest direct wave, while reflections from the boundaries or other structural features lead to weaker, delayed arrivals. Therefore, the predicted impact location is taken as the grid point with the maximum absolute amplitude over time according to Equation 2.17

This criterion is supported by the physical relationship between amplitude of the recorded fundamental antisymmetric mode A0 and the out-of-plane displacement of the plate, through the transfer function of the sensor. Assuming linear response of the sensor the recorded amplitude is proportional to the local displacement.

Yu et al. [27], adopted the same criterion for their impact localization, but the wave back-propagation was performed in the time domain. Pahlavan [26] identified the AE source location by finding the location where the wavefronts of the back-propagated signals first intersected.

Equation 2.17 is evaluated through a brute force searching process that involves reconstructing the wavefield at every point of a spatial grid covering the monitored area. For each candidate source point $\mathbf{x}_S$, the signals from all receivers are individually back-propagated using Equation 2.15, and then linearly superposed.

The reconstructed wavefield at each grid point is transformed in the time domain via the inverse Fourier transform, shown in Equation 2.18.

$$P(t) = \frac{1}{2\pi} \int_{-\infty}^{\infty} \hat{P}(\omega) e^{i\omega t} d\omega \tag{2.18}$$

This results in $S_{rec}(\mathbf{x}_S, t)$ for all grid points, from which the criterion given in Equation 2.17 is applied to obtain $\mathbf{x}_S$

An alternative approach which treats the localization process as an optimization problem is discussed in Section 6 as a potential future improvement.

2.3.5. Limitations of the Methodology

Impact localization in steel plates and stiffened panels using virtual TR is a straightforward and general approach. However, its performance depends on several practical factors which are pointed and discussed below.

The accuracy of GUW focusing is influenced by the spatial coverage of the sensors. Inadequate sensor coverage leads to false focusing and increased localization error. Additionally, accurate knowledge of the dispersion characteristics and structural geometry are necessary for the reconstruction of the wavefield. Simplifications in the modeled geometry and assumptions on the material properties may hinder the focusing process.

The methodology is also sensitive to noise and overlapping wavemodes. In the performed experiments, signal acquisition was set to *Normal Trigger* mode, where the sensors record signals when a predefined voltage threshold is exceeded. False triggers caused by noise corrupt the time synchronization between channels and make wavefield reconstruction impossible. Moreover, if a propagating wavemode is not accounted for in the phase delay term, its contribution distorts the focal point after the backpropagation of the recorded signals.

Finally, the localization accuracy is constrained by the grid resolution of the discretized wavefield reconstruction domain. While a finer grid improves localization precision as shown in Chapter 4, it also increases computational cost and dense grids become prohibitive for large scale structures.

2.3.6. Summary

This chapter presented the methodology developed for impact source localization in plates and stiffened panels using the TR property of GUW. The approach consists of an experimental and an analytical part.

During the experimental part, guided waves generated by artificial AE sources such as PLBs and instrumented hammer impacts, are recorded using PZT sensors. Single mode propagation is used

throughout the methodology for source localization and in the pre-processing step, the relevant A0 wave mode is isolated.

The analytical framework relies on a frequency domain formulation of GUW propagation, incorporating both dispersion and geometric spreading. In the case of stiffened plates, additional attenuation from structural features is modeled using a scalar transmission coefficient T_c.

Finally, source localization is achieved by virtually back-propagating the recorded signals from all sensors across a grid of potential source locations. The point of maximum reconstructed amplitude is selected as the estimated source, based on the assumption that constructive interference occurs only at the true source location. This approach is expected to work also in case of multiple focal points due to reflections from defects or boundaries, since the strongest focusing event, meaning the one that released the most energy, is selected as the source.

The key simplifications performed are single mode propagation, isotropy, negligible material damping, and flat sensor response across the frequency range of interest. The simplified modeling process is sufficient for the present work. Nevertheless, the methodology is not limited by these assumptions and simplifications, and can be extended to incorporate frequency dependent sensor transfer functions, frequency and orientation dependent T_c through the stiffeners, and multiple mode propagation.

3

Experiments

3.1. Small Scale Laboratory Experiments

The aim of the small scale experiments was to evaluate signal acquisition and the time reversal localization accuracy in a simplified geometry, and assess how different impact sources, namely Pencil Lead Breaks (PLBs) and an instrumented hammer affect signal quality and interpretation.

An overview of the experimental set-up is given in Figure 3.1. The test structure is depicted in 3.1a, it is a high tensile steel (S355) stiffened plate. The base plate measures 1700x1200x10 mm^3. The transverse stiffener is a 7 mm thick bulb profile and intersects with a longitudinal flange of 8 mm. Figure 3.1b depicts the acquisition set-up, each component has been given a number according to the path the signal follows.

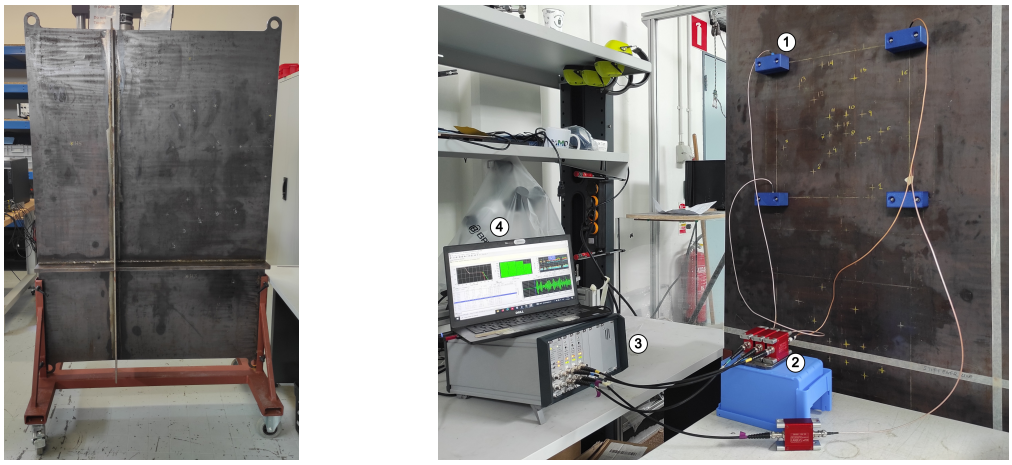

(a) (b)

Figure 3.1: (a) Steel stiffened plate. (b) Overview of the equipment used; (1) piezoelectric sensors, (2) pre-amplifiers, (3) Data Acquisition System, (4) Laptop with acquisition software

First the signal generated by the impact, propagates in the plate and reaches the piezoelectric (PZT) transducers. The signal is then amplified and recorded. The last step is signal processing, detailed in Chapter 4. In these experiments, commercial surface mounted r6α piezoelectric sensors, having 60kHz resonant frequency, manufactured by Physical Acoustics were used. The recorded signal is amplified using Vallen Systeme AEPH5 pre-amplifiers set to 40dB gain, before reaching the AMSY-6 Data Acquisition System (DAS) manufactured by Vallen Systeme.

3.1.1. Experimental procedure

Four surface mounted r6α piezoelectric sensors were placed in a square array enclosing a 400x400 mm^2 area on the back side of the plate allowing for convenient sensor placement and impact testing. Their positions, with respect to the origin as depicted in Figure 3.2 are listed in Table 3.1. Magnetic holders were used to secure the sensors in place and silicon grease was applied on the interface between the sensor and the plate to ensure proper coupling. Since, there is limited information in the literature regarding the frequency content of the stress waves emitted during medium scale impacts, it was assumed that the AE lie in the mid-frequency range, between 20 and 100 kHz. Therefore, the use of r6α sensors was considered a reasonable choice.

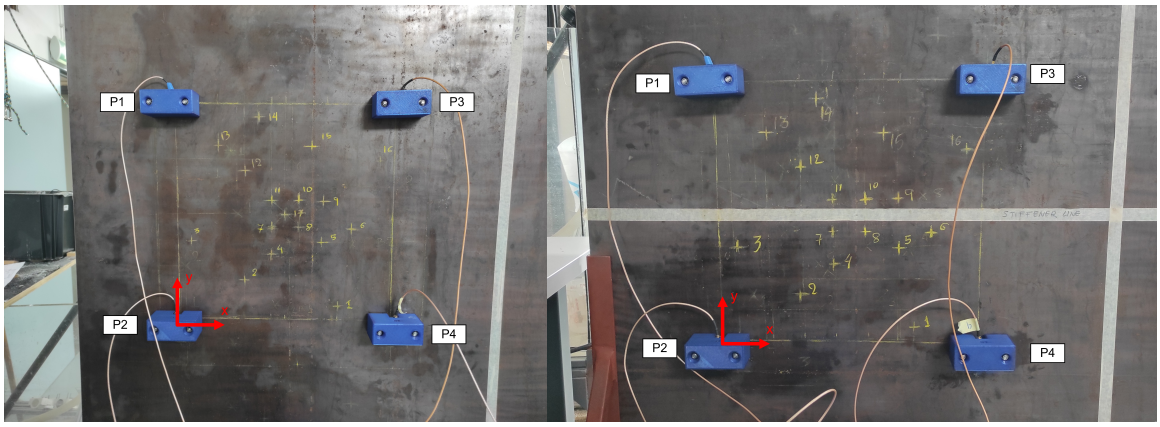

(a) Plate configuration

(b) Stiffened plate configuration with transverse bulb profile stiffener

Figure 3.2: Experimental set-ups for small-scale impact tests.

Table 3.1: Small scale experiments sensors position.

Sensor ID	sensor type	x [mm]	y [mm]
P1	r6α	0.00	400.00
P2	r6α	0.00	0.00
P3	r6α	400.00	400.00
P4	r6α	400.00	0.00

To investigate the effect of the stiffener on impact localization accuracy, two configurations were tested: a plate and a plate with a transverse stiffener introduced in the monitored area, as depicted in Figure 3.2. The plate configuration provides a baseline for TR localization in a homogeneous geometry, while the stiffened plate introduces geometric discontinuities that reflect and attenuate the propagating waves, potentially affecting localization accuracy. Notice, that the same set of sensors was used in all the experiments to avoid introducing further uncertainty from their different response.

AE signals were generated at predefined locations with PLBs and an instrumented hammer. These locations are listed in Table 3.2 and for clarity, they are also marked in Figure 3.3. The impact locations were chosen to evaluate localization accuracy at various distances from the sensors.

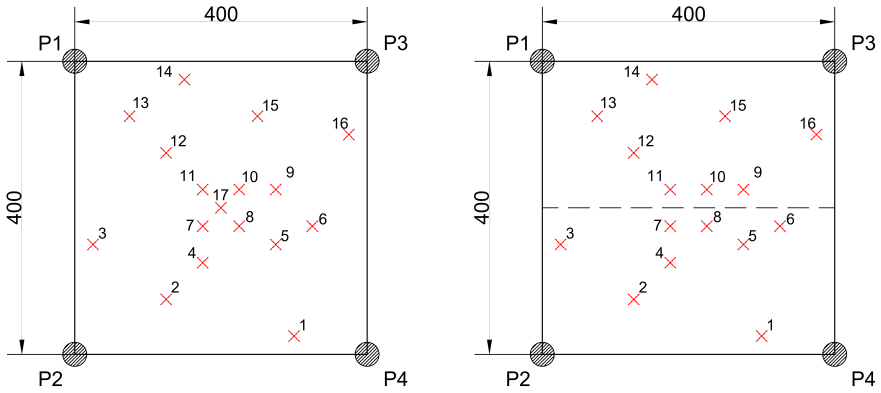

Figure 3.3: Impact test locations for small scale experiments. Left is the plate configuration and right is the stiffened plate configuration, the dashed line represents the stiffener.

Table 3.2: Small scale impact test locations

Location	x (mm)	y (mm)
1	300	25
2	125	75
3	25	150
4	175	125
5	275	150
6	325	175
7	175	175
8	225	175
9	275	225
10	225	225
11	175	225
12	125	275
13	75	325
14	150	375
15	250	325
16	375	300
17	200	200

Regarding the data acquisition (DAQ) Vallen Systeme's multi channel AMSY-6 and its corresponding software were used. The system was set to *Normal Trigger* mode, meaning that each sensor records a signal only when a user defined threshold is exceeded. The threshold is set based on the background noise, the energy of the impact and the size of the monitored area to avoid false triggers. To ensure that no information is lost, a *pre-trigger time*, namely how many samples prior to the trigger point will be stored, is set. The settings used on these experiments are listed in Table 3.5.

Table 3.3: Data Acquisition System settings.

Sample Rate [MHz]	Samples per set [-]	Threshold [dB]	Pre-trigger [μs]
10	16384	50	400

3.1.2. Acoustic Emission Sources

AE are triggered by sudden changes in the structures stress distribution. In isotropic materials such changes typically occur by impacts and crack growth. Two different AE sources were chosen to create stress waves, PLBs and instrumented hammer hits.

PLBs are widely employed to simulate AE signals generated by damage mechanisms such as crack initiation and growth. They produce short pulses, with the frequency content spread among a wide frequency range while the instrumented hammer generates longer-duration signals that last several ms, with most of their energy is concentrated in lower frequencies.

Pencil Lead Break (Hsu Nielsen Source)
A widely used substitute for AE events in laboratory experiments that offers both repeatability and practicality is the PLB, also known as the Hsu-Nielsen source, proposed by Arved Nielsen [43]. This method is standardized in ASTM E976 - 10. The required equipment consists of a mechanical pencil fitted with 0.35 or 0.5 mm diameter graphite leads of 2H hardness and a guide ring to maintain a constant contact angle against the structure under consideration, a schematic of this method is shown in Figure 3.4.

The mechanical pencil and its guide enable accurate placement and consistent break angles. In addition, keeping constant lead protrusion, usually 3 mm, ensures that duration and the force of the break and therefore the generated elastic waves remain consistent. Given the repeatability and simplicity PLB is a convenient tool for feasibility studies on source localization.

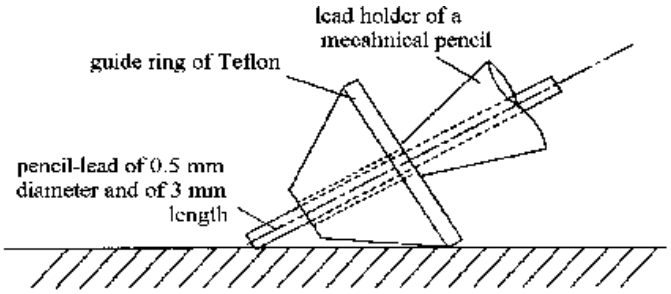

Figure 3.4: Schematic of Pencil Lead Break [44].

Instrumented Hammer
Instrumented hammers are commonly used for natural frequency identification and modal analysis. However, in the present study, they are chosen to serve as a more realistic impact source compared to the PLBs. The hammer consists of a piezoelectric IEPE force sensor which outputs a voltage signal, which is then converted to force using a transfer function provided by the manufacturer. It should be noted that IEPE sensors require current to operate, therefore, the hammer was connected to a Sirius 16 HD DAQ manufactured by Dewesoft, which offers this capability.

The hammer used in the current tests is shown in Figure 3.5, it is an IH-02 IEPE Instrumented Impact Hammer by DJB Instruments and has 2000N measuring range. Different impact tips can be attached to the impact hammer to adjust the impact impulse width and frequency response, therefore a set of rubber, nylon, aluminum and steel tips was available for this sensor. Given that the PZT sensors used to record the impact have a resonant frequency of 60kHz, the steel tip was used to maximize the energy content at higher frequencies. Steel on steel contact produces short duration impact signals, leading in broadband excitation in the frequency domain. Impacts performed with the impact hammer are less consistent and repeatable since they heavily rely on the user's technique to control the hit angle, duration and force. On the other hand, PLBs follow a standardized procedure and they are more repeatable, making them a common baseline for simulating AE events.

(a) DJB IH-02 Instrumented hammer

(b) Close-up of hammer tips; nylon (left) and steel (right)

Figure 3.5: Experimental set-ups for small-scale impact tests.

To ensure comparability between the two AE sources, the impact experiments were performed at the same locations in both configurations. Seventeen (17) and and sixteen (16) impact locations for the plate and the stiffened plate respectively, were distributed across the monitored area to assess the localization accuracy at various distances from the sensors.

3.1.3. Recorded Signals

In this section, representative signals recorded during PLB and impact hammer experiments are presented. For clear presentation the signals are plotted in the order of ascending time delay relative to the first trigger. All signals are aligned in time accordingly. Sensor i corresponds to Channel i ($i = 1 \ldots 4$).

PLB impacts (Location 4).

Figure 3.6 shows raw time domain signals for the two configurations tested, for an impact at location 4. Arrival order follows source–sensor distance, as expected for an isotropic plate. Sensor 2 being the closest triggers first while sensor 3 being the furthest triggers last. Despite proximity, Channel 1 continuously exhibits the largest amplitude in the plate tests, most likely due to sensor-specific electromechanical sensitivity.

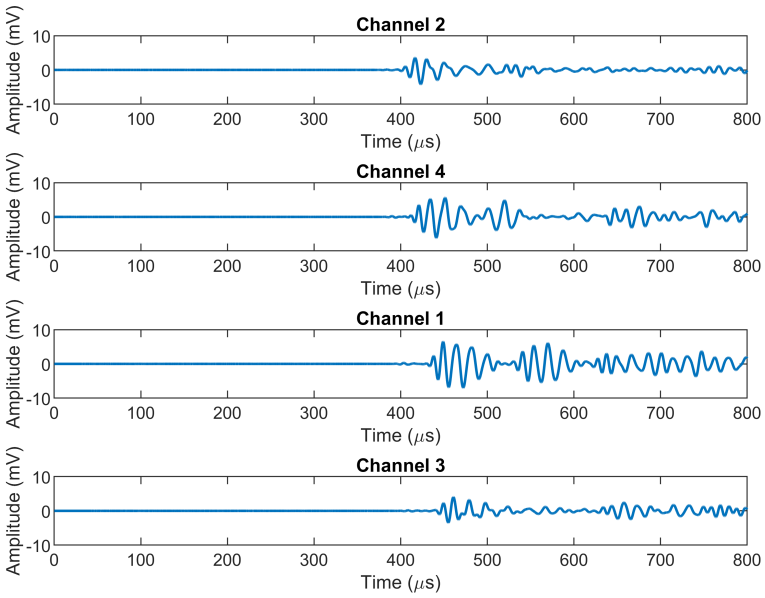

Figure 3.6: Flat plate: Raw sensor signals for PLB at Location 4.

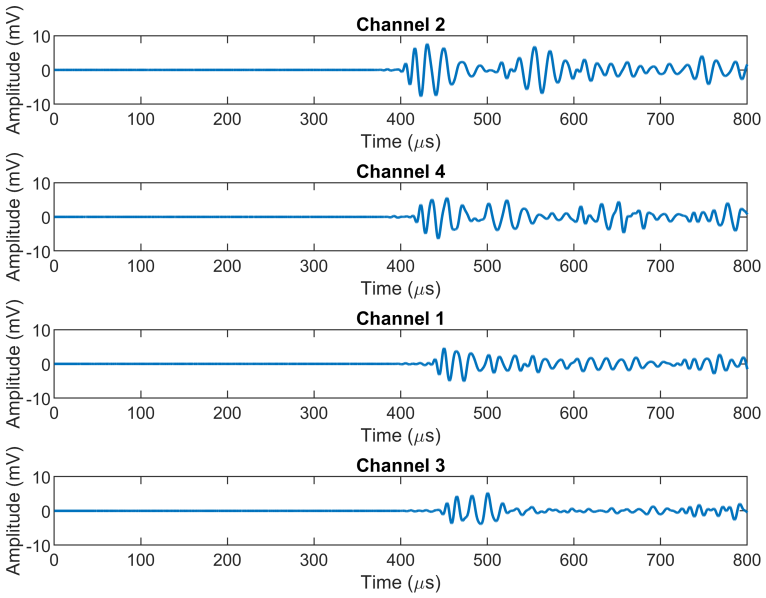

Figure 3.7: Stiffened plate: Raw sensor signals for PLB at Location 4.

Figure 3.7, shows the signals obtained in the stiffened plate configuration. Introducing the stiffener reduces the amplitude in Channel 1, whereas the amplitude of Channel 3 remains fairly unchanged. In the stiffened plate, multiple secondary packets, mainly noticed in Channels 2 and 4, indicate wave reflections and scattering at the stiffener.

Figure 3.8 shows the normalized spectra of these signals. The signals are denoised by a bandpass filter between 30 and 100 kHz. Adding the stiffener produces a clear shift of the dominant peak frequency and lowers frequency content in the range above 80 kHz in all channels. Channels 2 and 3 shift from ~47 to ~57 kHz, while Channel 4 shifts from ~57 to ~46 kHz. Part of the spectral change is also due to altered boundary conditions, in the stiffened setup, Sensors 2 and 4 the bottom boundary of the plate which is held by the steel frame as shown in Figure 3.1a.

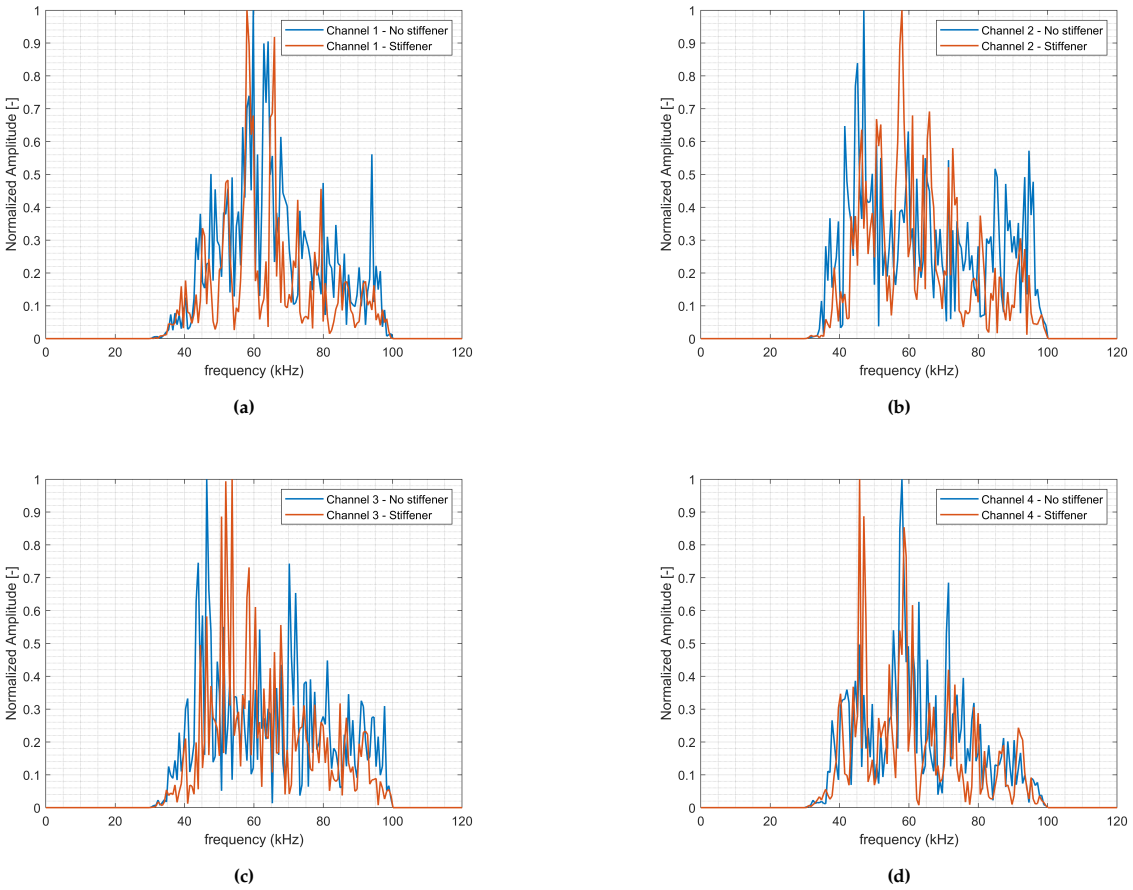

Figure 3.8: Normalized spectra for PLB at location 4: (a) Channel 1, (b) Channel 2, (c) Channel 3, (d) Channel 4. A bandpass filter between 30 and 100 kHz has been applied for visual ease.

Hammer impacts (Location 4).
Figures 3.9 and 3.10 show the signals obtained during the instrumented hammer experiments. Higher amplitude and more complex signals due to greater energy input are observed. Because plate and stiffened plate data come from different hits, absolute amplitudes are not compared. Later arrivals carry more energy than in the PLB case, suggesting that the increased input energy leads to sustained propagation and multiple reflections.

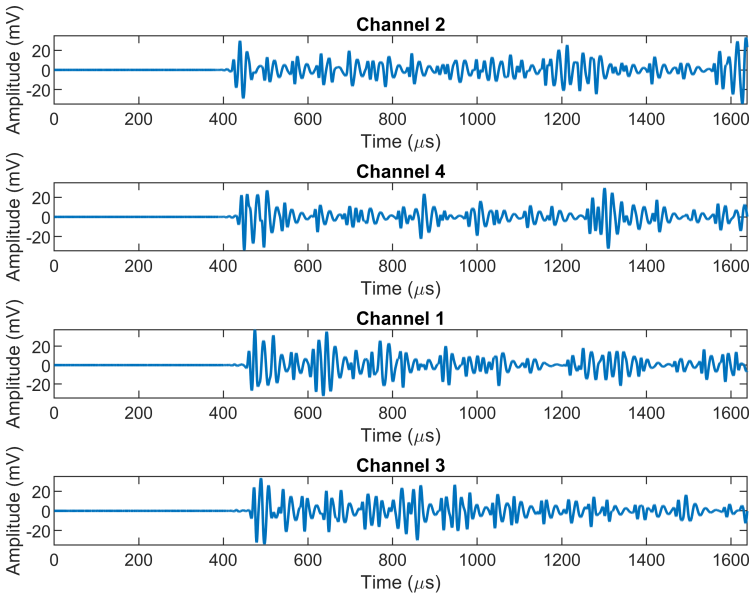

Figure 3.9: Flat plate: Raw sensor signals for instrumented hammer impact at Location 4.

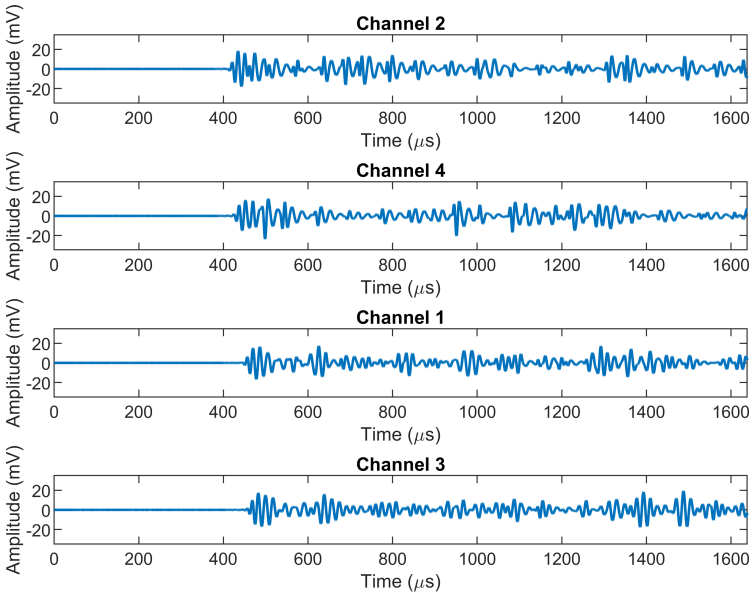

Figure 3.10: Stiffened plate: Raw sensor signals for instrumented hammer impact at Location 4.

The spectra illustrated in Fig. 3.11 exhibit much smaller peak shifts than PLB tests, and energy above 80 kHz is strongly attenuated in both configurations. For consistency, the same bandpass filter between 30 and 100 kHz is applied.

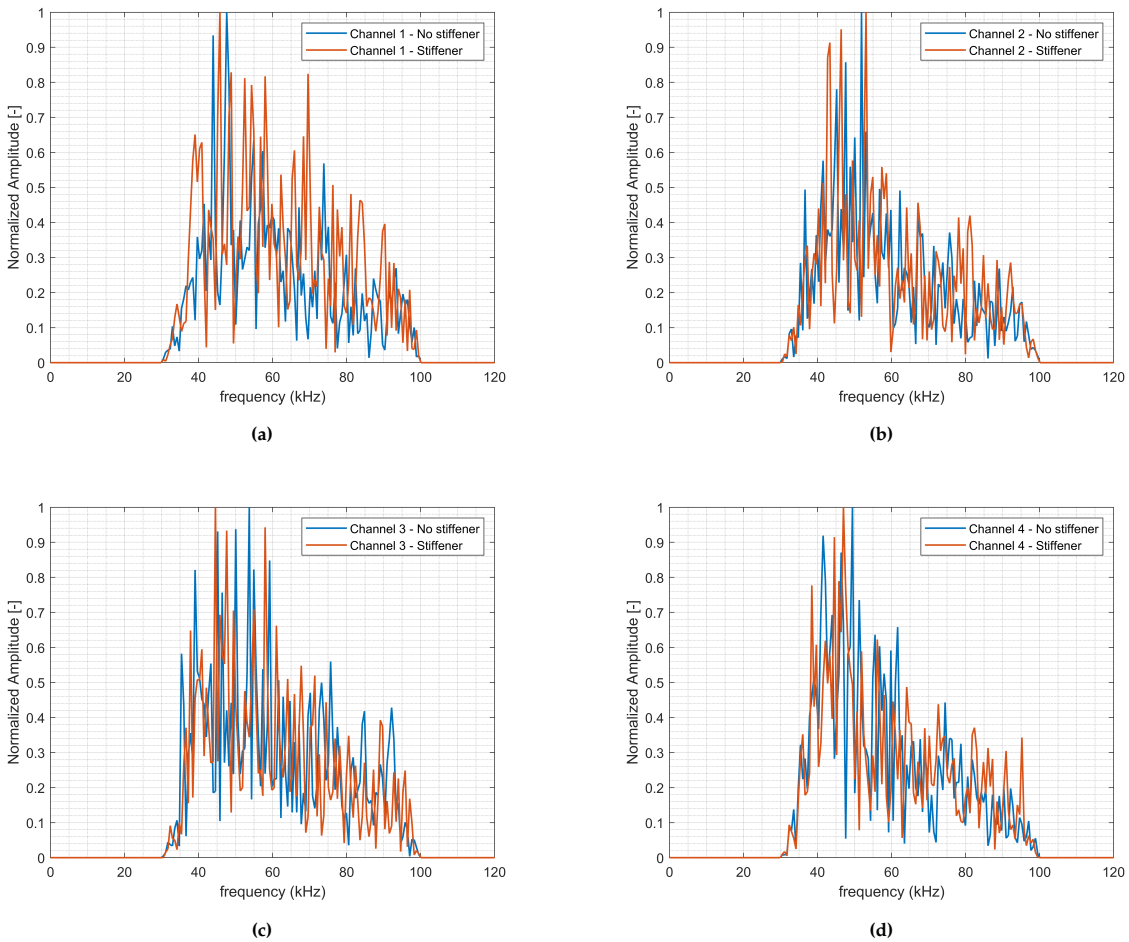

Figure 3.11: Normalized spectra for hammer impact at location 4: (a) Channel 1, (b) Channel 2, (c) Channel 3, (d) Channel 4. A bandpass filter between 30 and 100 kHz has been applied for visual ease.

3.2. Large Scale Experiments

The objective of the large scale experiment is to evaluate the applicability of the virtual TR based impact localization methodology discussed in Chapter 2 on an actual ship structure and assess the performance of commercial piezoelectric sensors for a realistic monitored area.

3.2.1. Test Structure Description

The experiments were conducted onboard a Shoalbuster vessel under construction at DAMEN Shipyards in Gorinchem, shown in Figure 3.12. The Shoalbuster is a multipurpose tug being approximately 35 m in length with a draft of about 4 m. The monitored structure is shown in Figure 3.13, and is the port sideshell plating inside the engine room of the ship. Multiple vertical stiffeners and web frames are included, forming a stiffened panel with non-uniform plate thickness and geometric irregularities. The monitored area spans 7500 mm in length and 2000 mm in height.

Figure 3.12: External view of the Shoalbuster vessel at DAMEN Shipyards in Gorinchem.

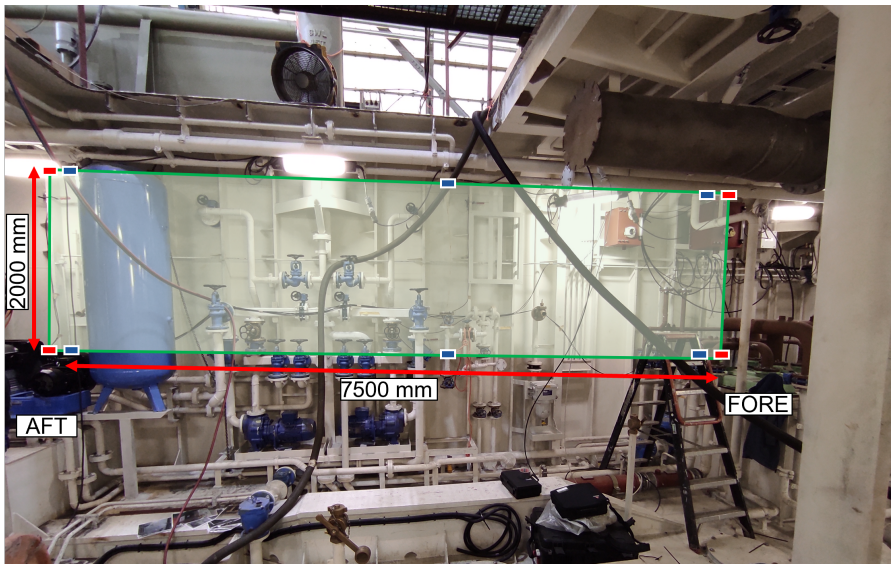

Figure 3.13: Monitored structure onboard Shoalbuster. The rectangle depicts the monitored area, the blue filled rectangles represent the 60 kHz sensors and the red the 30 kHz sensors.

A drawing was developed based on measurements taken on board, frame numbering and the reference coordinate system are chosen arbitrarily, and do not correspond to the actual ship reference system. The drawing is added below in Figure 3.14 and is used as reference.

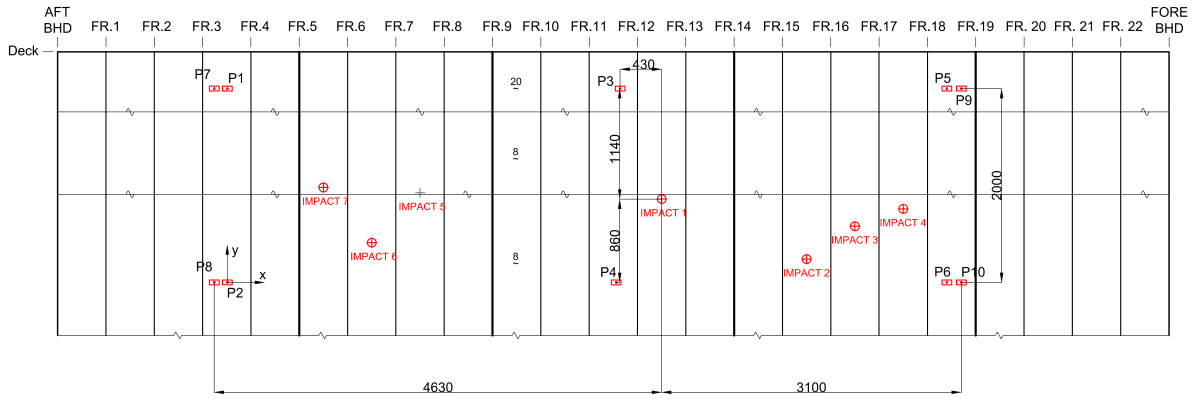

Figure 3.14: Structural Drawing of monitored area. The impact and sensor locations are marked with red.

3.2.2. Instrumentation and Sensor Layout

A total of ten (10) surface mounted PZT sensors were used over the monitored area. The sensor array consists of six (6) r6α with 60kHz central frequency corresponding to sensors P1 to P6, and 4 r3α sensors with 30 kHz central frequency corresponding to sensors P7 to P10 as shown in 3.14, all manufactured by Physical Acoustics. These two types of sensors were deployed to evaluate their performance and determine which is more appropriate for impact localization in large structures.

The placement strategy of the sensors was designed to ensure adequate coverage of the monitored area. The higher resonant frequency r6α sensors were placed on the corners of the monitored area and toward the center, while the lower resonant frequency r3α sensors were positioned only on the corners of the monitored area. This is based on the understanding that lower frequency components are less prone to attenuation over long distances, thus lower frequency sensors can cover larger areas. The position of each sensor according to the origin of Figure 3.14 is listed in Table 3.4.

Table 3.4: Large scale experiments sensors position.

Sensor ID	sensor type	x [mm]	y [mm]
P1	r6α	0	2000
P2	r6α	0	0
P3	r6α	4065	2000
P4	r6α	4065	0
P5	r6α	7500	2000
P6	r6α	7500	0
P7	r3α	-150	2000
P8	r3α	-150	2000
P9	r3α	7650	2000
P10	r3α	7650	0

Each sensor was mounted on the structure using magnetic holders manufactured by Mistras, and was coupled with silicon grease, to ensure proper detection of the ultrasonic waves. The sensors were connected with SMA cables to AEP5H pre-amplifiers by Vallen Systeme set to 40 dB gain, which were either placed on flat surfaces or clamped on the vertical stiffeners using F-clamps. To protect the pre-amplifiers from mechanical damage during the installation process thin rubber layers were placed between the F-clamp and the device. Indicative pictures of the placed sensors and the securing of the preamplifiers are shown in Figure 3.15.

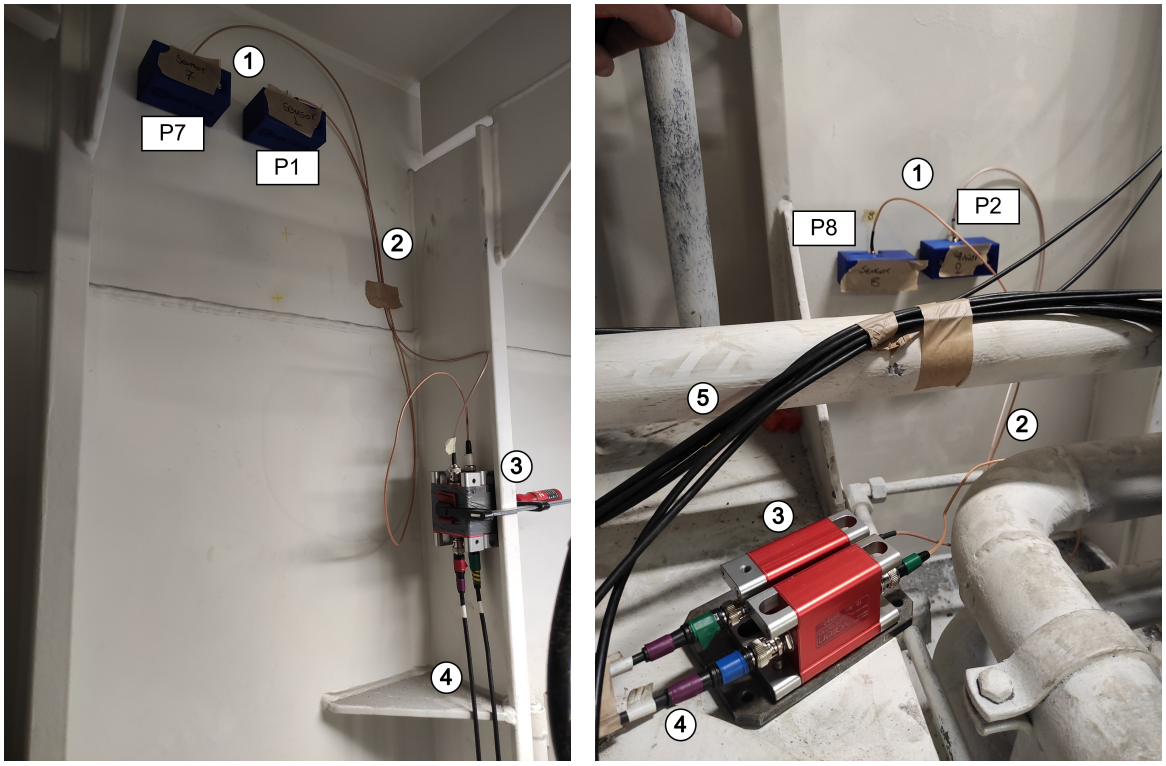

(a) (b)

Figure 3.15: Sensor and pre-amplifier placement. (1) PZT sensor, (2) SMA cable, (3) AEP5H preamplifier, (4) co-axial BNC cable to DAQ, (5) routed co-axial BNC cables from other sensors to DAQ.

3.2.3. Data Acquisition Configuration

The amplified signals were sent to the AMSY-6 DAQ by Vallen Systeme via coaxial BNC cables. The DAQ, shown in Figure 3.16 supports simultaneous multi channel acquisition for up to 20 channels, making it suitable for this large scale set-up. The routing of the BNC cables was decided on site, and was such as to not obstruct the steel works that took place parallel to the experiment.

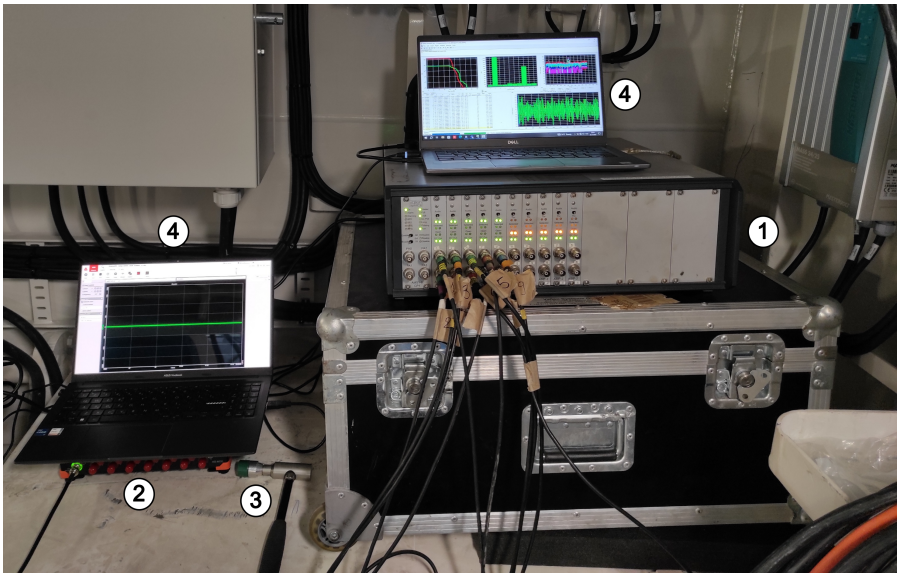

Figure 3.16: Data Acquisition System. (1) AMSY-6 DAQ, (2) Sirius 16 HD DAQ, (3) PCB Piezotronics impact hammer, (4) Laptops with the DAQ software.

To ensure compatibility with the expected signal durations and to minimize file size, a sampling rate of 5 MHz was chosen. The signal length was configured to 32,768 samples, corresponding to a total duration of 6,553.6 μs. This extended signal length was selected to make sure that the concurrent propagation of fast S0 and slower A0 wave modes, if present, would be captured, especially at large distances where wave mode separation becomes more pronounced.

Triggering was set to *Normal Trigger* mode, meaning each sensor only recorded signals when the amplitude exceeded a user defined threshold. A trigger threshold of 50 dB was selected based on the background noise and the required sensor sensitivity. This value was chosen also on prior findings by Saccone and Pahlavan [33] which suggests that stiffeners can attenuate signal amplitudes up to 5 dB per crossing. A pre-trigger of 500 μs was set to ensure the initial parts of the signal were not missed.

The rearm time, which corresponds to the minimum period between two distinct events on the same channel, was set to 250 μs. Although this value was effective for the small scale experiments it might not have been the optimal ideal in large scale structures where tests where wave packets arriving later due to reflections and longer travel paths could be misinterpreted as new events.

Table 3.5: Large Scale Experiments - Data Acquisition System settings.

Sample Rate [MHz]	Samples per set [-]	Threshold [dB]	Pre-trigger [μs]
5	16384	50	400

3.2.4. Test procedure and Execution

Two different impact hammers were used to perform controlled impacts on the structure, a DYTRAN Instruments 5803A hammer and a PCB Piezotronics 086D05 hammer, shown in Figure 3.17, both fitted with hard tips to produce high-frequency content. The DYTRAN hammer, being larger and heavier, generated higher-energy impacts with long durations, approximately 10 ms. Its higher mass also made it more prone to generating double hits, because the structure's elastic deformation caused the hammer to strike twice, complicating signal interpretation and leading to the generation of multiple AE events for the same impact. The PCB hammer, being lighter, produced shorter-duration impacts of approximately 3 ms, a duration similar to what was observed in lab.

(a) (b)

Figure 3.17: (a) PCB Piezotronics 086D05 and (b) DYTRAN 5803A instrumented hammers.

Before performing test impacts, the setup was validated using PLBs near each sensor. These checks

confirmed that all sensors could register signals in the vicinity of 90 dB, indicating good coupling and system readiness.

Seven impact locations were selected across the monitored area. They were marked on the exterior of the hull using reference points such as Frame 9, where a bollard sits, and the known thickness change seam. For redundancy, the same set of impacts was repeated inside the hull. Due to spatial constraints such as valves, pipes and cables, only the smaller hammer could be used in the interior of the ship. The impact locations and sensor layout were documented using photos, videos and schematic diagrams to support reproducibility. Table 3.6 lists the impact locations.

Table 3.6: Large scale impact test locations

Location	x (mm)	y (mm)
1	4495	860
2	5995	240
3	6495	580
4	6995	785
5	1995	925
6	1495	410
7	995	980

During the impact tests, shipyard activities such as welding, grinding, and cutting, taking place concurrently, resulted in elevated background noise levels. As a consequence, numerous AE events unrelated to the controlled impacts were recorded. In several cases, AE hits were triggered but did not receive a Transient Recorder Index (TRAI), indicating that while the system detected the events, no associated waveform data was stored. As a result, only a subset of events discussed in Chapter 5 is analyzed in this work.

3.2.5. Recorded Signals

In this section a few raw recorded signals are presented, the signals are plotted in the order of ascending time delay relative to the first trigger. Figure 3.18 shows the signals recorded form the r6α sensors and Figure 3.19 shows the signals recorded from the r3α sensors, for an impact performed with the PCB Piezotronics hammer at location 1.

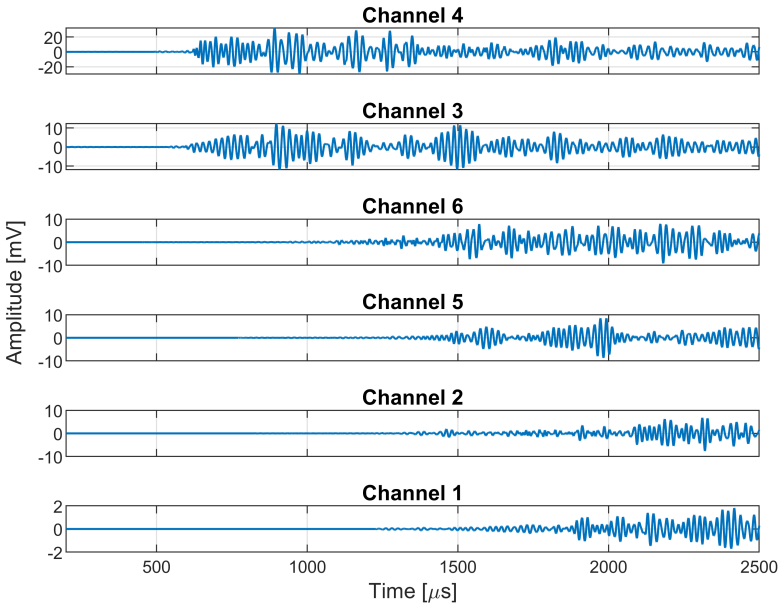

Figure 3.18: Raw signals recorded from r6α sensors for an impact at location 1.

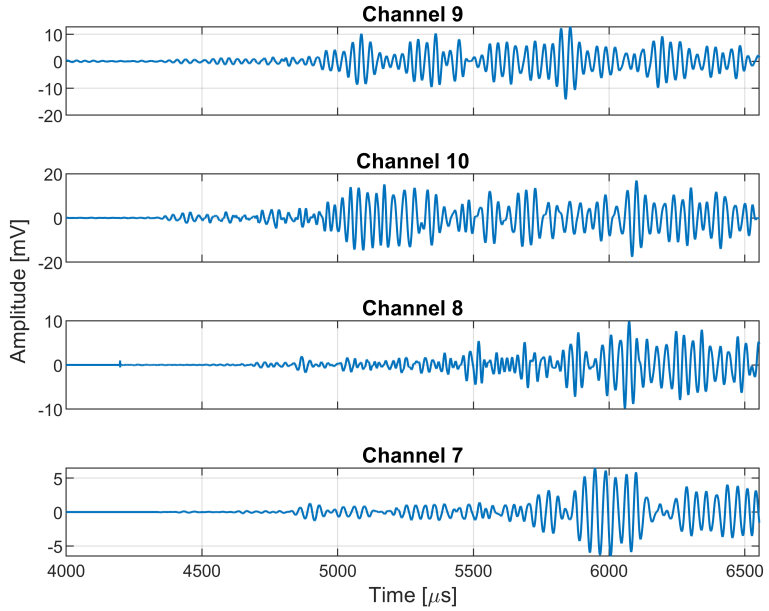

Figure 3.19: Raw signals recorded from r3α sensors for an impact at location 1.

The arrival order reflects the source–sensor distances. Sensors 3 and 4, are the closest and trigger first and sensors 1 and 2 which are the furthest trigger last. Regarding the r3α array, sensor 9 appears to be triggered prematurely by noise and recorded only 1 ms of data, aligning the other r3α sensors with respect to the early trigger, results in a delay of 4.5 ms in the valid waveforms.

4

Virtual TR Implementation

4.1. Overview

This chapter details the MATLAB implementation of the virtual TR process theoretically described in the Methodology in Chapter 2. Figure 4.1 summarizes the numerical workflow, from signal pre-processing to source localization.

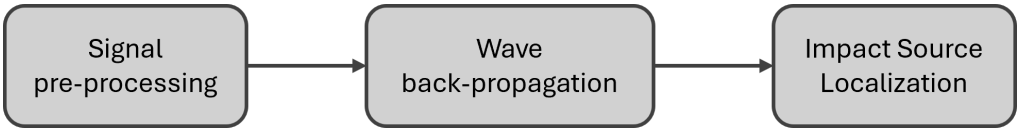

Figure 4.1: Workflow for numerical implementation of TR based source localization.

4.2. Small-scale Processing & Simulation

4.2.1. Signal pre-processing

Prior to TR, recorded signals are pre-processed to synchronize the individual sensor recordings, isolate the fundamental antisymmetric wave mode (A0) which dominates the recorded signals and suppress unwanted signal components.

Time Alignment

As described in Chapter 3 each channel is triggered independently, hence absolute recording start times differ. The earliest trigger time is selected as temporal reference. Every other recorded signal $P_i(t)$ is phase-shifted in the frequency domain according to Equation 4.1, to achieve signal synchronization.

$$P_i(\omega) \rightarrow P_i(\omega) \cdot e^{-i\omega\Delta t_i} \tag{4.1}$$

where, $P_i(\omega)$ is the Fourier transform of the recorded signal and Δt_i is the difference in trigger time between the reference channel and the current channel i.

Window Function

To suppress reflections and unwanted propagating modes a time window is applied around the A0 wave mode arrival. A flat top window with cosine shaped flanks is used. The length of these smooth transition flanks is one tenth of the total window length on either side. A fixed length window of 100 μs was chosen for all the numerical simulations on the small scale set-up. This window adequately isolates the A0 wave mode.

Figure 4.2, shows the pre-processed signals with respect to the distance from the AE source. For visualization clarity, the distances shown on the vertical axis are not to scale. A dashed line is overlaid to represent a linear fit through the zero crossing points immediately preceding the peak amplitude of

the direct arrival at each channel. This fit and known distance between each sensor and the impact provides an estimate of the group velocity. The calculated velocities are listed in Table 4.1. The estimated velocities adequately agree with the theoretical group velocity of 3076.20 m s^{-1} shown in Figure 4.3.

Table 4.1: Estimated group velocities from zero–crossing fits (Location 4).

Source type	Configuration	v_g (m/s)
PLB	Flat plate	3025.1
PLB	Stiffened plate	2833.8
Hammer	Flat plate	2830.8
Hammer	Stiffened plate	2922.8

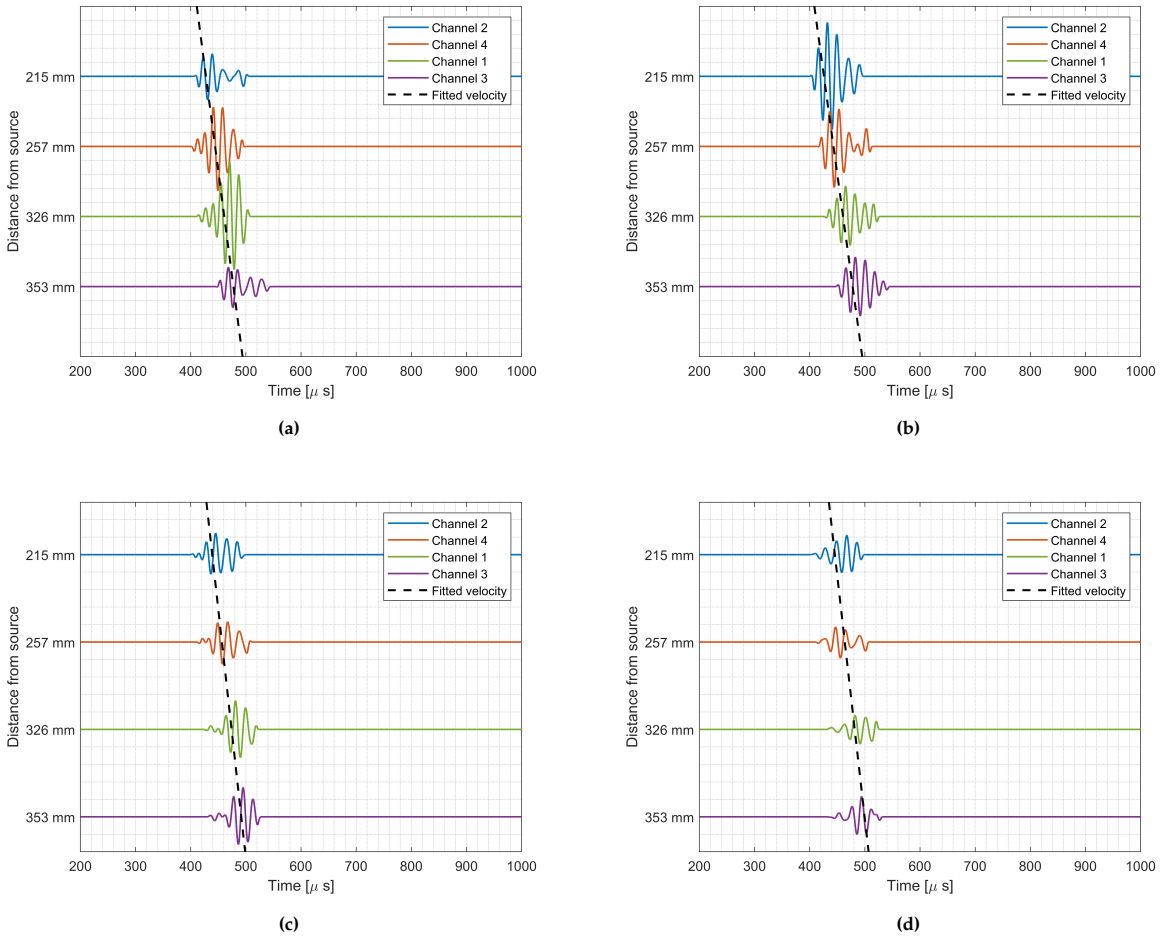

Figure 4.2: Indicative estimated group velocity in the small scale configuration. (a) PLB flat plate, (b) PLB stiffened plate, (c) Hammer impact flat plate, (d) Hammer impact stiffened plate.

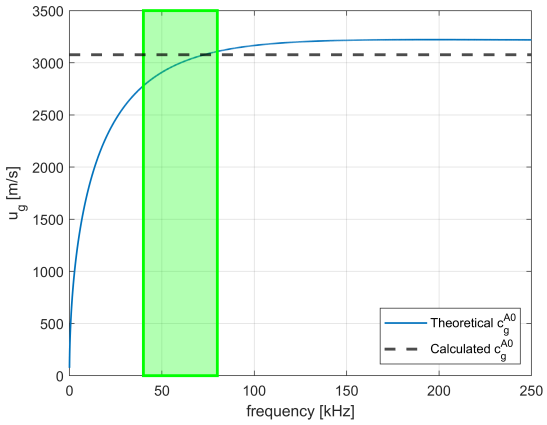

Figure 4.3: Theoretical A0 wave mode group velocity

Band-pass Filtering

A trapezoidal band-pass filter with sloped transitions is used to retain the frequencies where the PZT sensors exhibit uniform sensitivity while rejecting low and high frequency components associated with structural vibrations and noise respectively. The filter used in these simulations is presented in Table 4.2, and is centered around 60 kHz, which is the central frequency of the sensors.

Table 4.2: Bandpass filter

Lower stop	Lower pass	Upper pass	Upper stop
40 kHz	45 kHz	75 kHz	80 kHz

4.2.2. Grid Convergence Study

The monitored surface is discretized on a uniform $\Delta x \times \Delta y$ grid (Figure 4.4a), according to literature $\Delta x < \lambda_{\min}/2$. In the small scale experiment set-up, $\lambda_{\min} = 23.2$, mm for a 10, mm steel plate (Figure 4.4b). Nevertheless, a grid-convergence is performed to choose the optimal grid resolution.

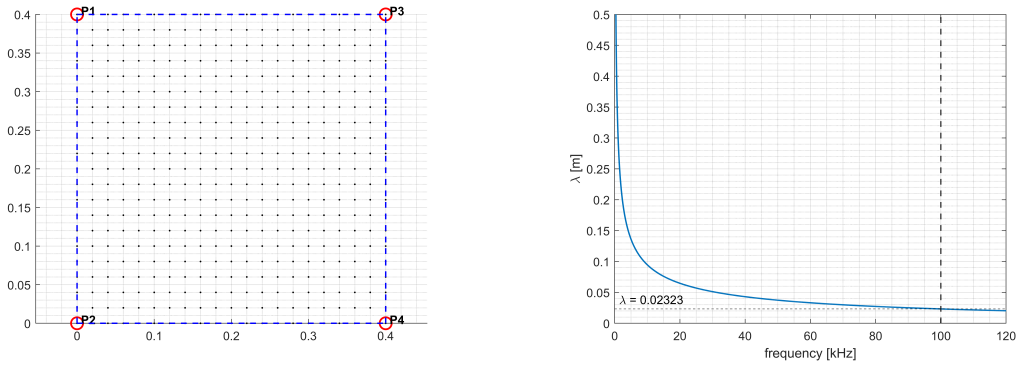

(a) Rectangular plate discretization

(b) A0 wavelength

Figure 4.4: Indicative 2D grid on rectangular plate and A0 wavelength for a 10 mm steel plate

The grid convergence study was performed using the Pencil Lead Break (PLB) at Location 4 on the flat plate configuration. The virtual TR process was executed with decreasing grid sizes, and the relative distance between successive predicted source locations was monitored. The simulation is considered converged when the relative difference between two consecutive predictions is less than 5 %.

The outcomes are summarized in Table 4.3 and the relative difference and localization error are plotted in Figure 4.5. It is observed that for a grid spacing of $\Delta x = 4$ mm the change compared to the previous (5 mm) case is approximately 1.55 %, satisfying the convergence criterion. In addition to mesh convergence, the absolute localization error, defined as the Euclidean distance between the predicted and actual impact locations, was also evaluated. The 4 mm mesh meets the convergence criterion and results in a localization error of 8.7 mm, whereas the 5 mm and the 3.2 mm mesh sizes predict the impact location with an error of 11.92 mm and 10.76 mm respectively. Therefore, 4 mm resolution is chosen as it balances numerical stability and localization accuracy.

Table 4.3: Convergence Study Summary

Δx [mm]	x_{pred}	y_{pred}	Relative Difference [%]	Localization Error [mm]
10.00	174.30	133.30	-	8.33
8.00	179.59	114.29	8.99	11.65
5.00	177.22	136.71	10.59	11.92
4.00	177.78	133.33	1.53	8.78
3.2	177.42	135.48	0.98	10.76

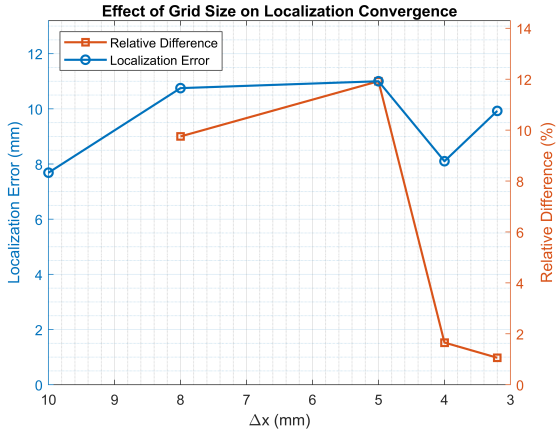

Figure 4.5: Grid convergence study.

4.2.3. Wavefield Reconstruction

The wavefield is reconstructed by virtually propagating the recorded signals to each grid point. Wave propagation is modeled through the analytical approximation discussed in Chapter 2.

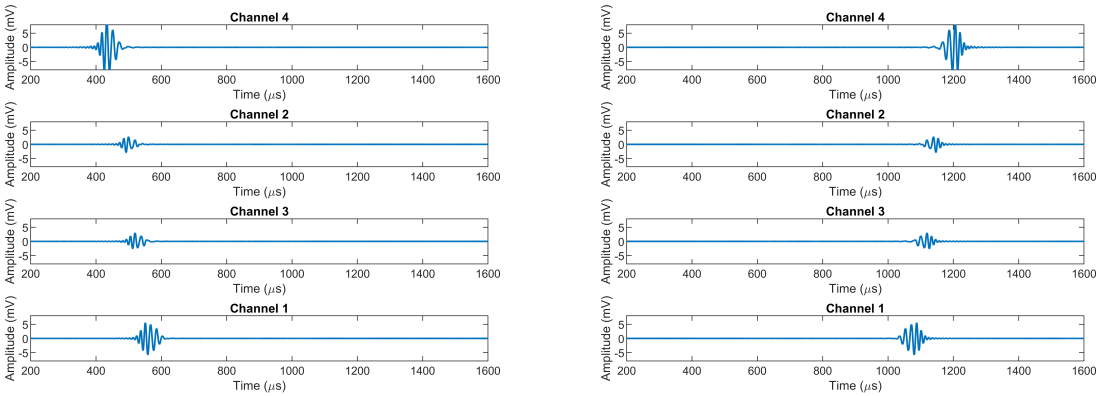

Figure 4.6: Pre-processed signals. (a) Recorded signal; (b) Time Reversed signal.

Figure 4.6 plots the pre-processed signals recorded during the PLB experiment at Location 1 on the plate configuration before and after time reversal. Notice, that the signal which recorded last is now emitted first, which is explained by the fact that this wave is required to cover longer distance to trace back to the impact location.

By linearly superimposing the the wavefield created by each sensor yields the reconstructed wavefield snapshots shown in Figure 4.8. The wavefield develops according to the emission sequence of the time reversed signals.

At the first timestamp, the back propagated energy radiates only from Sensor 1 Figure 4.8a. By the second time stamp the dominant contribution comes from Sensor 1 but the wave propagating from Sensor 3 is visible, followed sequentially by Sensors 2 and 4, Figures 4.8c and 4.8d, progressively reconstructing the wavefield.

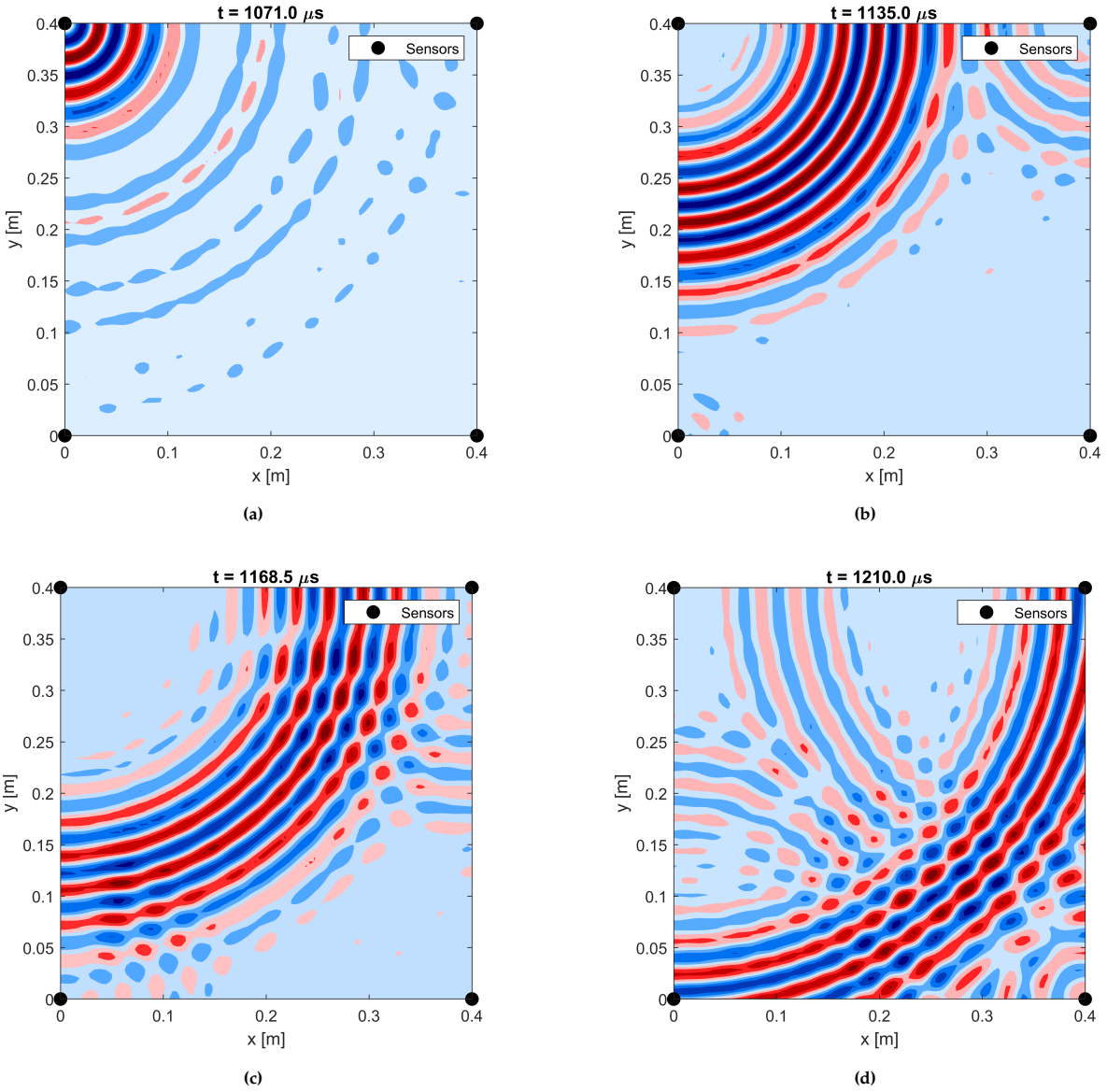

Figure 4.7: Simulated wave propagation at selected timestamps.

4.2.4. Impact Source Localization

The described reconstruction process results in a time trace on every grid point. The impact location is then predicted by finding the coordinates where E, being the amplitude of the reconstructed signal,

obtains its maximum value over time as shown in Equation 4.2.

$$E(x, y) = \max_{t} |u(x, y, t)| \tag{4.2}$$

The Figures below, depict the reconstructed wavefield for both configurations at the time where the maximum amplitude occurs. The predicted and actual impact locations are overlaid, the stiffener is plotted as dashed line.

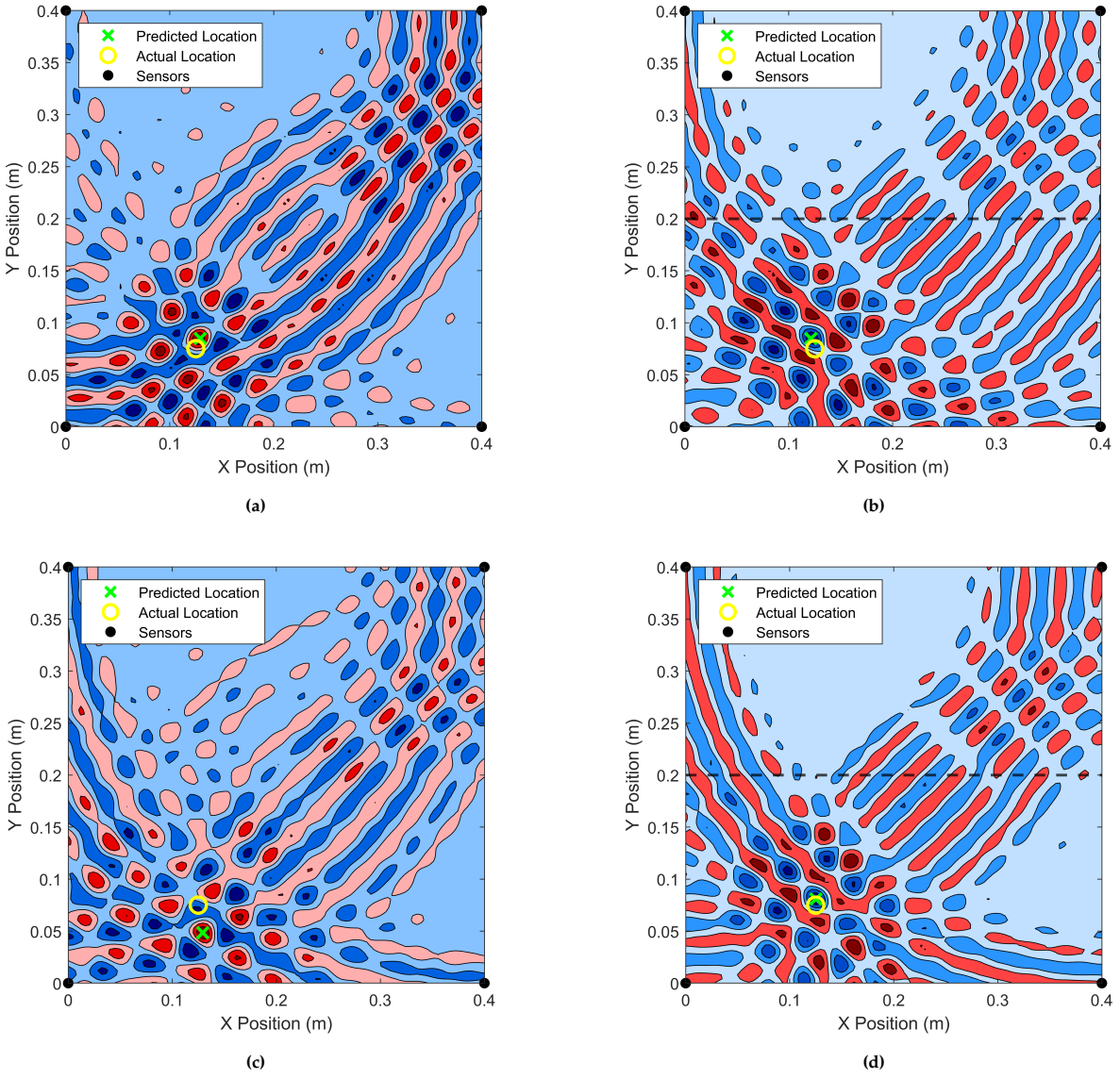

Figure 4.8: Simulated wave propagation at selected timestamps.

4.2.5. Alternative Localization Approach

Beyond the exhaustive grid search described above, an alternative approach would be to treat source localization as an optimization problem since the wave propagation function is well defined across the plate. Specifically, the aim would be to search for the source point $\mathbf{x}_S$ that maximizes the TR cost function given in Equation 4.3.

$$F(\mathbf{x}_S) = \sum_{\omega} \left| \sum_{i=1}^{N} \frac{P_i^*(\omega) W(\mathbf{x}_S, \mathbf{x}_R, \omega)}{T_c} \right|^2 \tag{4.3}$$

where, i is the number of sensors used to reconstruct the wavefield.

This procedure can be implemented with numerical optimization algorithms that search for the maximum iteratively in without evaluating the function on every grid point. Such methods significantly reduce computational time, since exhaustive calculations are avoided and accuracy is increased since it is not limited by the grid size. On the other hand, such approaches sensitive to the initial guess required in the optimization problem and prone to the misinterpretation of local maxima as the impact source, especially in complex structures where multiple focal points are expected.

In contrast, evaluating the function on every grid point and exhaustively searching for the maximum guarantees that the global maximum is found, which agrees with the description of TR theory. Finally, it produces heatmaps that help in the interpretation of the reconstructed wavefield.

4.3. Large Scale Simulations

4.3.1. Signal pre-processing

The data collected during the large-scale experiments were subjected the same pre-processing routine described in Section 4.2.1, however bandpass filtering and signal windowing were adapted to account for the differences in sensor types and signal length and quality.

Window Function

The flat-top window with cosine flanks described in Section 4.2.1 was employed to isolate the portion of the signals for time reversal. Due to the complexity and long duration of the recorded waveforms, as well as the elevated noise levels during testing, the direct arrivals associated with the impact are ambiguous. Additionally, channels were likely triggered by unrelated acoustic events, making the first threshold crossing unreliable as a windowing reference. Consequently, the time window was not defined relative to the trigger time, as done in the small-scale experiments.

Instead, a fixed 1 ms segment was extracted from the beginning of each signal. This duration was selected because it is likely to include the wave packets related to the impact. This approach introduces later reflections and unrelated AE events in the TR process, however it serves as a practical solution for the given experimental conditions.

Band-pass Filtering

The trapezoidal band-pass filter with sloped transitions described in Section 4.2.1 is used to isolate the frequencies where the PZT sensors exhibit uniform sensitivity while rejecting low and high frequency components associated with structural vibrations and noise respectively. As described in Chapter 3, two types of sensors with central frequencies of 30 and 60 kHz were used. The applied bandpass filters are presented in Table 4.4 and 4.5.

Table 4.4: Bandpass filter for r6*a* sensors

Lower stop	Lower pass	Upper pass	Upper stop
40 kHz	45 kHz	75 kHz	80 kHz

Table 4.5: Bandpass filter for r3*a* sensors

Lower stop	Lower pass	Upper pass	Upper stop
20 kHz	25 kHz	55 kHz	60 kHz

4.3.2. Wavefield Reconstruction

The process for wavefield reconstruction discussed in the previous section is applied again here. The TR procedure inherently compensates for dispersion because each frequency component is back-propagated with its own $c_{\mathrm{p}}(\omega)$. However, the analytical model used to simulate guided wave propagation needs to be adapted to account for the non-uniform plate thickness. More specifically, the distance between

a sensor and a grid point must be decomposed into segments corresponding to regions of different thickness, and the appropriate dispersion curves must be used for each segment, as described in Equation 2.9.

No grid convergence study was performed for this set-up. The localization process takes place in two steps. The location is first estimated using a 20 x 20 mm^2 coarse grid. Then, the region where the location was predicted is discretized with a denser 10 x 10 mm^2 grid, satisfying the criterion suggesting that $\Delta x \leq \lambda/2$, leading to a more accurate prediction. Figure 4.9, shows the minimum wavelength for a A0 waves propagating in plates with 8 and 20 mm thickness.

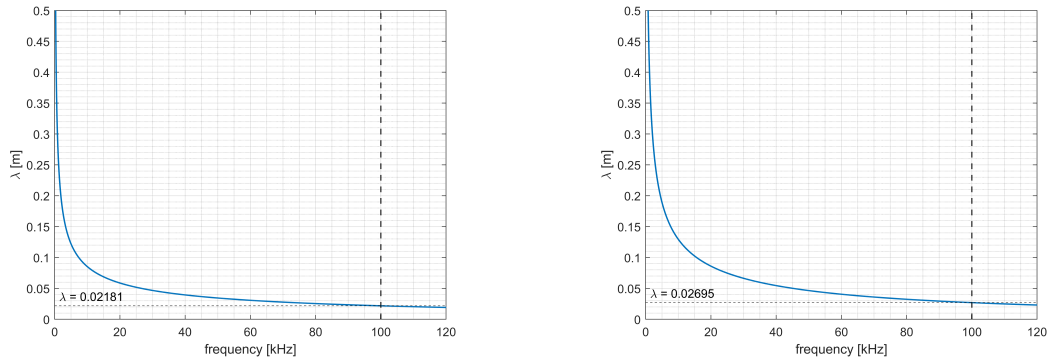

(a) 8 mm plate **(b)** 20 mm plate

Figure 4.9: A0 mode wavelength for plates of different thickness.

The Figures below, depict the reconstructed wavefield at the time of the impact using different sensor combinations for an impact performed at location 1.

Figures 4.10a and 4.10b, show the reconstructed wavefield using the r6α sensors 1, 2, 5 and 6 for a grid size of 20 x 20 and 10 x 10 mm^2 respectively. The horizontal axis limits in Figure 4.10b extend from 4.065 m to 7.5 m. The different propagation characteristics due to different plate thickness are clearly visible in Figure 4.10b, where the waves in the top strip (above Y ≈1750 mm are traveling with higher velocity.

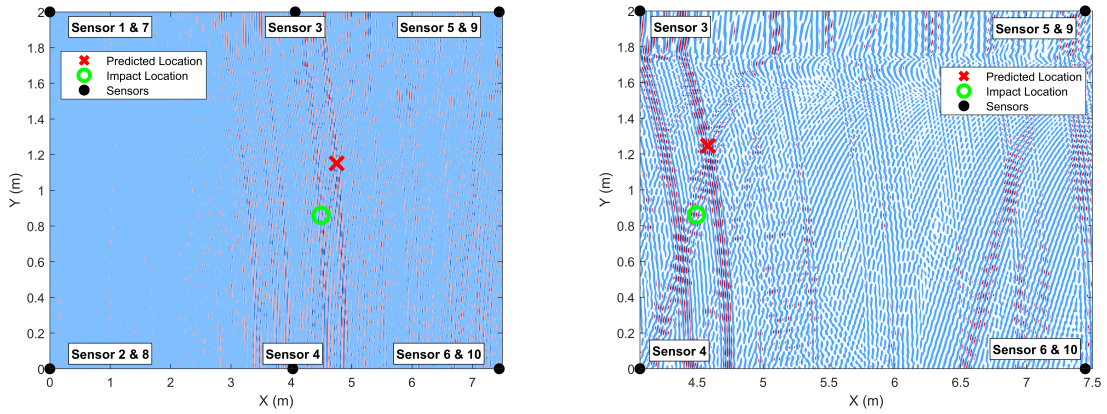

(a) **(b)**

Figure 4.10: Impact localization using sensors 1,2,5 and 6 for (a) 20x20 mm^2 and (b) 10x10 mm^2 grid.

Figure 4.11a shows the reconstructed wavefield using the r6α sensors 3, 4, 5 and 6 for a grid size of 10 x 10 mm^2. Figure 4.11b shows the reconstructed wavefield using the r3α sensors 7, 8, 9 and 10 for a grid size of 20 x 20 mm^2, a simulation with a denser grid was not performed for this case as focal point .

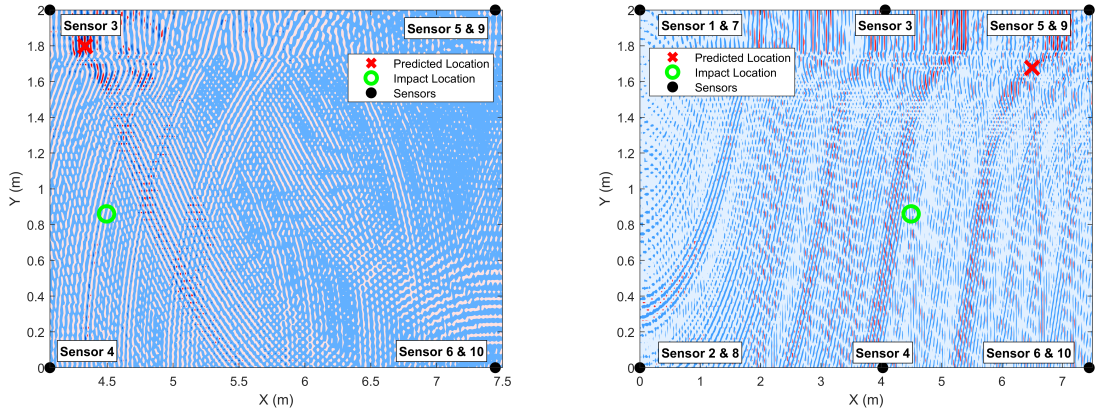

(a) (b)

Figure 4.11: Impact localization using sensors (a) 3, 4, 5 and 6 (b) 7, 8, 9 and 10 for a (a) 10x10 mm^2 and (b) 20x20 mm^2 grid.

4.4. Limitations

The implementation of virtual TR presented in this chapter is subject to the limitations arising from the assumptions made in modeling.

First, single mode propagation using only the fundamental antisymmetric mode (A0) excludes the contribution of the fundamental symmetric mode (S0) which cannot always be fully excluded during windowing, especially in short propagation distances. The residual S0 content is therefore back-propagated using the A0 dispersion curves, resulting in incorrect phase delay terms potentially leading to localization errors. Similarly, the assumption of flat, frequency independent and identical sensor transfer functions neglects the variations between sensors which in practice result in amplitude and phase inconsistencies.

The effect of the stiffeners is incorporated through a scalar transmission coefficient $T_c = 0.65$. This value is selected based on the experimental results published by Saccone and Pahlavan [33] presented in Chapter 1.5. This value is representative for a broad range of angles of incidence, however a decrease in the transmission coefficient was observed for incidence angles exceeding 140 °. A full sensitivity analysis was not performed in this work but exploratory tests, in the small scale setup with T_c in this order of magnitude had little influence on the predicted location. In large models with multiple stiffeners however, the compound stiffener effect might significantly influence the localization accuracy. Nevertheless, future work should investigate an angle dependent transmission model to more accurately capture the stiffeners effects.

Finally, the current implementation requires prior knowledge of the impact location for the manual application of the transmission coefficient T_c along the correct propagation paths. Specifically, the propagation paths between the impact point and the sensors are known in advance, and the corresponding signal amplitudes are selectively scaled when a stiffener is crossed for each simulation. While this approach is acceptable at this stage for developing the methodology, it limits the model's applicability in real world scenarios. In a true impact experiment, the location of the impact is unknown and the effect of structural components should be incorporated in the model without relying on manual adjustments.

5

Results and Discussion

5.1. Overview

In this chapter the source localization results are reported and discussed. The data was collected during the experimental campaigns summarized below.

- **Small scale Experiments** plate and stiffened panels configurations measuring (0.4 m×0.4 m) tested with PLBs and instrumented hammer.
- **Large scale Experiments** stiffened panel measuring (7.5 m×2.0 m) with multiple stiffeners and realistic boundary conditions.

In each case the localization error is calculated as the Euclidean distance between the true impact point (x_{true}, y_{true}) and the predicted impact point (x_{pred}, y_{pred}), as shown in the equation below.

$$\Delta = \sqrt{(x_{\text{pred}} - x_{\text{true}})^2 + (y_{\text{pred}} - y_{\text{true}})^2} \tag{5.1}$$

5.2. Source Localization Results - Small Scale Experiments

During the small scale experiments two configurations were tested. The first consisted of impacts on a plate and the second consisted of impacts on a stiffened plate. Two different AE sources were used, PLBs and an instrumented hammer to perform more realistic impacts. The data collected during the experimental stage was pre-processed and back propagated virtually to reconstruct the wavefield at the time of the impact, as described in the Chapter 4.

A total of 102 impacts were performed on the plate configuration, 51 per source type and 96 on the stiffened plate, 48 per source type. Figures 5.1a–5.2b show the localization error for each impact location and configuration. Three impacts per location were performed. Individual errors are plotted as light blue dots, the mean error as a red diamond, and the dashed line at 40 mm marks the 10% error threshold relative to sensor spacing.

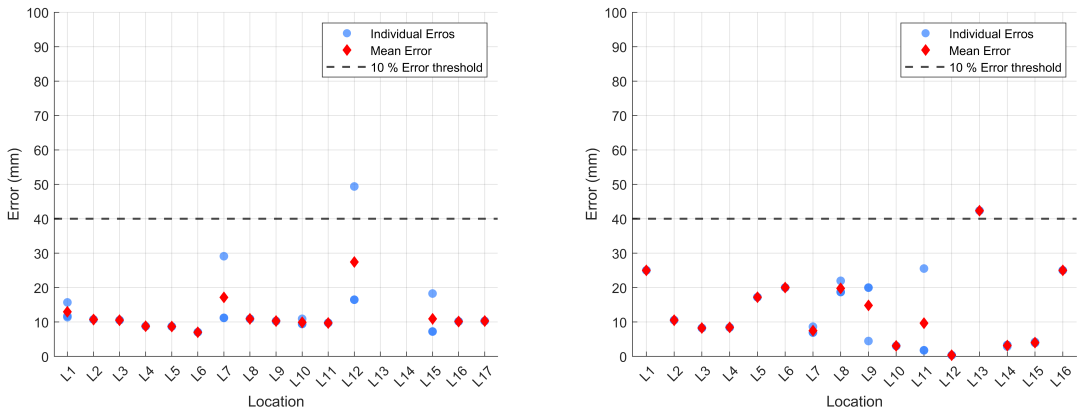

(a) Flat plate **(b)** Stiffened plate

Figure 5.1: PLBs - localization error

For the PLB experiments on the plate the mean error at 14 out of 17 locations lies below 20 mm which corresponds to 5% of sensor spacing. The mean error in this configuration, excluding the experiments at locations 13 and 14 is 11.71 mm with a standard deviation of 6.72 mm. On the stiffened plate, the mean error is slightly higher 12.45 mm with a standard deviation of 10.28 mm, but still well below the 10% threshold. It is also noticeable that the large error noticed at locations 13 and 14 for the plate configuration is eliminated. Nevertheless, location 13 is still predicted with larger error compared to the other experiments.

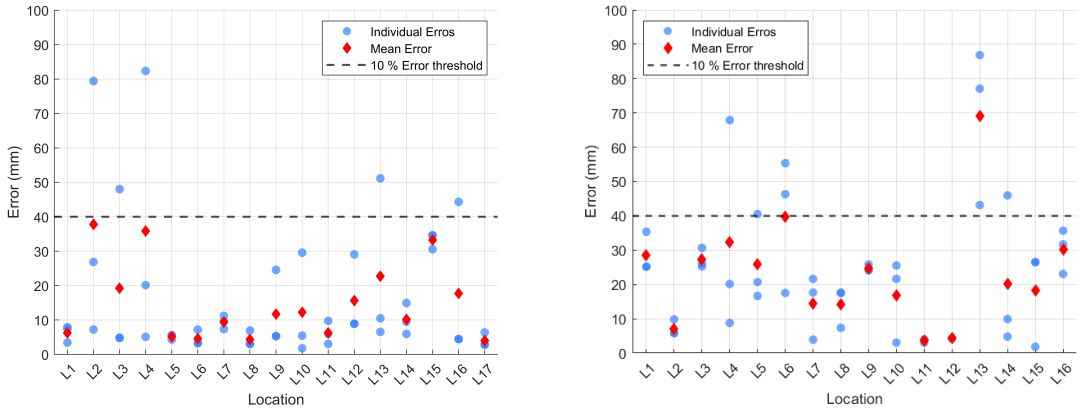

(a) Flat plate **(b)** Stiffened plate

Figure 5.2: Instrumented hammer impacts - localization error

As far as the instrumented hammer impacts are concerned, it is observable that the errors are generally higher and more variable. Plate configuration shows a mean error of 15.08 mm with a standard deviation of 18.24 mm, while the localization error in the stiffened plate configuration increases to 23.54 mm with a standard deviation of 19.15 mm. It should be noticed however, that individual errors sometimes exceed 80 mm. The larger standard deviation values compared to the ones calculated for the PLB experiments, reflect the inherent variability of the hammer impacts due to differences in impact energy, duration, and angle.

5.3. Source Localization Results - Large Scale Experiments

Localization performance in large scale was evaluated across five impacts performed on three distinct locations. At least three impact tests were performed at each location listed in Chapter 3 Table 3.6, but many signals were lost. In the context of this work, the impact tests to be analyzed are two (2) impacts at

location 1, one (1) impact at location 5 and two (2) impacts at location 7, all performed with the PCB Piezotronics instrumented hammer. The coordinates of these positions with respect to the origin which coincides with the coordinates of P2 as shown in Figure 5.3 are listed for completeness in Table 5.1.

Table 5.1: Analyzed impact test locations for large scale experiments

Location	x (mm)	y (mm)
1	4495	860
5	1995	925
7	995	980

The localization accuracy is examined across four different sensor arrays, each one representing a different combination of sensors, in an effort to assess the appropriateness of each sensor type and array configuration.

Group 1 consists of four r6α sensors placed at the corners of the monitored area. Specifically, Sensors 1, 2, 5, and 6. Group 2 also uses four r6α sensors, but includes combinations of corner and midpoint sensors. Two configurations fall under this group: the first consists of Sensors 1, 2, 3, 4 while the second group has Sensors 3, 4, 5, and 6, selected depending on which subset encloses the impact location. Group 3 is composed of four r3α sensors placed at the corners of the monitored area, namely sensors 7, 8, 9, and 10. Group 4 employs all six r6α sensors (Sensors 1 through 6), combining both corner and midpoint placements. Figure 5.3, illustrates the location of the sensors on the monitored area.

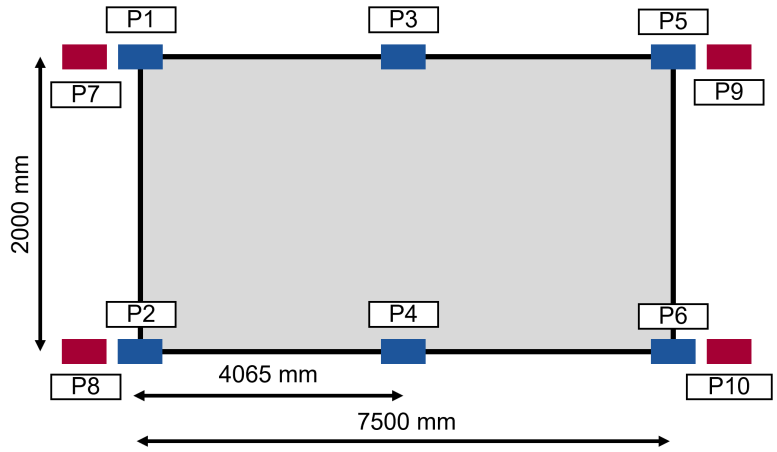

Figure 5.3: Monitored area and sensor positions. Blue rectangles correspond to r6α and red ones to r3α sensors.

An array with both r6α and r3α sensors was not tested, because from an engineering point of view in real world structures sensor uniformity is usually preferable . Additionally, different sensor types also have different transfer functions and that would require further calibration to ensure compatibility within the proposed methodology.

As discussed earlier, the localization error is defined as the Euclidean distance between the estimated and actual impact coordinates.

Table 5.2 summarizes the results of the impact localization for the experiments performed onboard the Shoalbuster, for the different sensor arrays.

Table 5.2: Large Scale Experiments localization results for different sensor arrays

Location	Test ID	Sensor Group	True X [mm]	True Y [mm]	Estimated X [mm]	Estimated Y [mm]	Error [mm]
1	1	Group 1	4495	860	4582.37	1246.23	395.99
	1	Group 2	4495	860	4336.40	1788.90	942.34
	1	Group 3	4495	860	6497.33	1676.70	510.00
	1	Group 4	4495	860	6697.79	1717.00	2363.62
	2	Group 1	4495	860	7058.80	1717.00	2703.24
	2	Group 2	4495	860	4138.48	222.20	730.68
	2	Group 3	4495	860	5855.61	1616.10	1556.58
	2	Group 4	4495	860	6697.86	1717.17	2363.75
5	1	Group 1	1995	925	922.46	686.87	1098.66
	1	Group 2	1995	925	2097.71	727.27	222.81
	1	Group 3	1995	925	962.57	1737.30	1313.68
	1	Group 4	1995	925	942.51	626.26	1094.06
7	1	Group 1	995	980	260.70	1939.39	1208.15
	1	Group 2	995	980	173.90	969.70	821.16
	1	Group 3	995	980	180.48	1717.17	1098.57
	1	Group 4	995	980	0.00	2000.00	1424.93
	2	Group 1	995	980	813.00	1171.72	264.35
	2	Group 2	995	980	1249.93	444.40	593.18
	2	Group 3	995	980	1455.64	1676.77	835.27
	2	Group 4	995	980	822.19	1717.17	757.15

Figure 5.4 shows the localization error for the large scale experiments for the four sensor array groups. Each colored marker corresponds to an individual test at a given location, while the red diamonds denote the mean error per group. The dashed black line at 1000 mm indicates the 10% threshold which is here chosen arbitrarily.

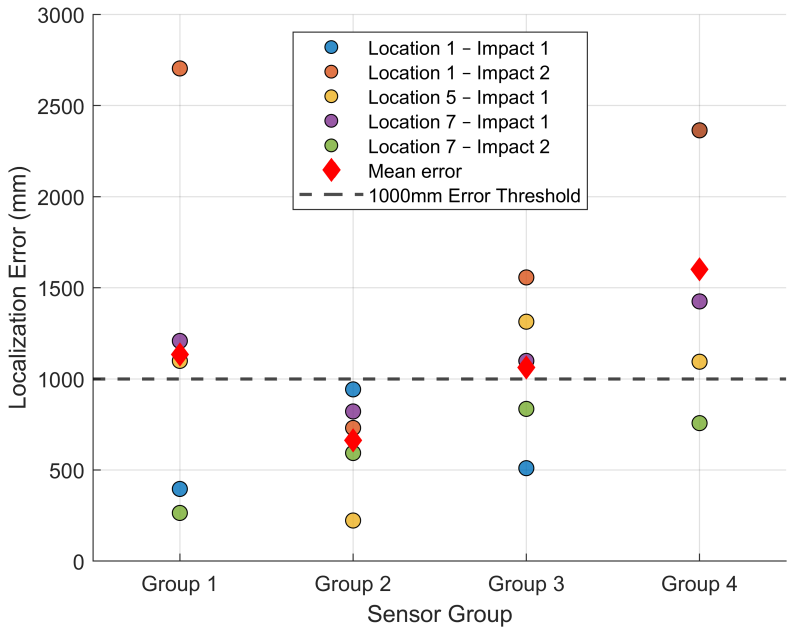

Figure 5.4: Localization Error for different sensor array configurations.

Group 2 shows the best performance, with mean localization error of 662 mm and relatively tight clustering of the individual results, indicating more consistent localization. Group 1 achieved low

individual errors in some cases, approximately lower than 400 mm, but also output the largest outlier exceeding 2700 mm, leading to a mean localization error of 1134 mm. Group 4, has lower accuracy compared to the other configurations consisting of 60 kHz sensors and predicts the impact locations with a mean error of 1230 mm. Finally, Group 3, consisting of the 30 kHz sensors achieves the lowest accuracy overall, with a mean localization error of 1393 mm. Impact localization with sensor groups 1, 3 and 4 also shows wide scatter, with individual and mean localization errors generally exceeding the threshold.

These findings indicate that the sensor array configuration has a strong influence on localization accuracy. Specifically, the denser configurations which in this case included midpoint sensors, and therefore split the monitored area in half, outperform the arrays with sparsely placed sensors Additionally, Group 2 not only predicts the impact location with the lowest mean error but also demonstrates the most consistent performance, with reduced error variability across all tests. This is visually confirmed in Figure 5.4, which presents individual localization errors and group mean errors for the different sensor configurations.

The mean localization error observed in the large scale experiments using a dense sensor array (Group 2) is comparable to that reported by Grabowski et al. [19], where AE localization was performed on a large gas tank. In their work, sensors were placed approximately 5 m apart, and the structure included a thickness transition from 8 mm to 10 mm along the height. Their analysis localized the source using a dispersion compensation approach assuming uniform plate thickness of 9 mm. The reported localization error was approximately 700 mm which is of the same order as the mean errors observed in the large scale experiments. They observed that the horizontal accuracy was in the order of a few mm and the major discrepancy was found in the vertical direction due to the thickness change, the results of the present research however do not agree with this observation.

5.4. Discussion

The results presented in this chapter suggest that virtual TR of GUW for impact localization method performs very accurately in controlled small scale tests but the accuracy is reduced in the large-scale experiments.

5.4.1. Interpretation of Results for the Small-Scale Experiments

Regarding the PLB experiments, the impact was localized consistently with low error and the low standard deviation in the predictions demonstrates the method's robustness under controlled excitation.

The focal points for impacts performed at locations 13 and 14 for the plate configuration were found significantly offset from true. In both cases Sensor 1 registered disproportionally higher amplitudes compared to the rest of the sensors in these experiments. As a consequence, during the back propagation, where the signal is further amplified by the division with the geometric spreading term, the wavefield recreated by sensor 1, dominated the wavefield reconstruction and led the waves to focus at the edges of the plate, furthest from this sensor, as shown in Figure 5.5a. To support this, the wavefield reconstruction was performed while neglecting the contribution of sensor 1 and the localization accuracy was improved significantly as shown in Figure 5.5b.

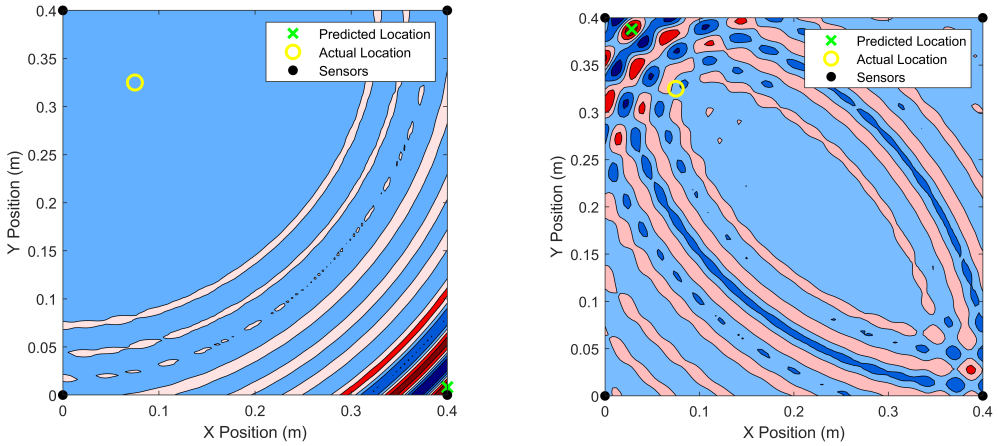

Figure 5.5: PLB localization at location 13. (a) Localization defocus, (b) improved localization removing the contribution of sensor 1.

Instrumented hammer impacts were predicted with higher mean localization error and standard deviation compared to the PLB experiments. This reflects the variability of the impacts in impact energy and contact angle and duration.

The presence of the stiffener also introduced additional complexity, as seen by the higher standard deviation in both PLB and hammer tests, highlighting the influence of structural discontinuities on the reconstruction of the wavefield. Nevertheless, the localization accuracy in all small scale experiments remained well within the 10% threshold with respect to sensor spacing, demonstrating that the method is robust under different test conditions and structures.

5.4.2. Interpretation of Results for the Large-Scale Experiments

In the large-scale experiments a reduction in the localization accuracy was observed. Dense sensor configuration (Group 2) achieved the lowest mean localization error of $\approx$ 662 mm. This error is comparable to literature values for experiments performed in a large tank of 10 m radius [19]. Other sensor configurations showed significantly larger individual as well as mean localization errors, which in some cases exceeded 2000 mm.

Figure 5.6 shows the extracted signal portions for an impact performed at location 7, aligned vertically based on the known impact location, note that the distances are not to scale. It can be observed that channels 5 and 6, which correspond to the sensors located furthest from the impact, are not correctly aligned in time with the rest of the channels. This is likely due to false triggering by background noise, which registered up to 80 dB during the shipyard experiments, especially from the sensors placed at the fore end of the monitored area. Channels 1 and 3 show earlier arrivals compared to channels 2 and 4, despite being at almost equal distances from the source. This is due to the higher wave velocity in the thicker plate sections, confirming the influence of non-uniform plate thickness on propagation.

Local velocity variation is compensated in the propagation model but erroneous signal synchronization limits the performance of virtual TR. A recommendation for future works would be to either try aligning the signals by cross correlation instead of threshold crossing timestamps or to change the trigger mode in the acquisition settings, such that when one channel is triggered then all channels start recording.

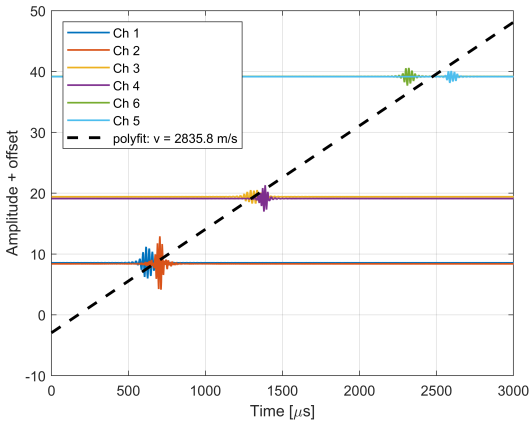

Figure 5.6: Processed signals recorded from impacts performed at location 7.

In addition, the scalar transmission coefficient T_c was kept equal in both the small and large scale experiments. While the stiffeners had similar geometric properties (HP 80x7 in small scale and HP 120x7 in large scale), a more detailed analysis should be performed to capture the angle dependence and the effect of the different boundary conditions in large structures.

Beyond the primary stiffeners, additional structural features, which were not modeled, such as brackets, holes, and pipe supports welded to the sideshell also introduced multiple scattering and reflections. These features increased the complexity of the wavefield and contributed to the observed reduction in localization accuracy.

Finally, as described in Chapter 4, the signal window used had a fixed duration of 1 ms. Reflections and noise were inevitably included in the virtual TR process and possibly distorted the wavefield reconstruction and reduced localization accuracy.

6

Conclusions and Future work

6.1. Conclusions

This thesis explored impact localization on plates and stiffened panels using TR of GUW signals. The approach combined experimental testing and numerical simulations. Experiments were performed at small and large scale, the former were carried out in the Structures lab of the Mechanical Engineering faculty at TU Delft, and the latter onboard a Shoalbuster under construction at DAMEN Shipyards in Gorinchem.

In the small scale experiments on plates the predicted impact locations exhibited small localization errors. More specifically the location of the Pencil Lead Breaks was predicted with a mean error of approximately 11.71 mm with a standard deviation of 6.72 mm excluding two cases where the waves focused close to the boundaries of the monitored area. For instrumented hammer impacts the mean localization error was 15.08 mm with a standard deviation of 18.24 mm. The larger variability is attributed to the less repeatable nature of hammer impacts and their dependence on force magnitude, contact duration and impact angle.

Regarding the stiffened plate experiments carried out in the laboratory, the results for PLB are similar to the plate configuration. Mean localization error of 12.45 mm and standard deviation of 10.28 mm were observed. Hammer impacts yielded higher errors averaging at 23.54 mm and standard deviation of 19.15 mm.

By normalizing the mean error with sensor placement distance one can observe that the error stays below 10 % suggesting that the presence of stiffeners can be reasonably approximated within the proposed model with a scalar transmission coefficient $T_c = 0.65$, applied as a frequency and path independent attenuation factor.

When the methodology was scaled from laboratory conditions to an actual ship structure localization accuracy decreased due to the increased structural complexity. The presence of multiple vertical stiffeners, web frames and secondary structural components such as brackets and cutouts created multiple reflections and reducing localization accuracy. Furthermore, concurrent steel works such as welding, grinding and cutting introduced significant acoustic noise and created false triggers, hindering the identification of the direct arrival of the wave emitted during the impact. Non uniform plate thickness further complicated signal interpretation and required adjustments on the propagation model.

Despite these challenges, the proposed approach achieved acceptable localization accuracy. Localization errors vary with sensor type and array configuration, ranging from approximately 220 mm to over 2700 mm. In general the arrays consisting of r6α sensors outperformed these of r3α sensors. In particular, arrays of r6α sensors placed roughly 4000 mm apart in the length direction and 2000 mm apart in the height direction achieved a mean localization error of 662 mm with individual errors tightly clustered compared to arrays with sparsely placed r6α and r3α sensors. Arrays with mixed sensors types were not tested considering that sensor uniformity is a practical requirement, in real world scenarios.

These findings demonstrate that the method can be extended to full scale applications where thickness variations and multiple stiffening components are present. Some degradation in performance is expected and can be mitigated through sensor placement and acquisition settings optimization. It should be noted that in absence of specific data, all vertical stiffeners were modeled using the scalar factor calculated for the laboratory setup in previous works [33]. A more detailed incorporating the transmission coefficient tailored to the actual structural components would likely improve accuracy further.

In summary, this work demonstrates that TR of a single GUW, in particular A0, is a feasible technique for impact localization in steel thin walled structures, from plates to complex ship hulls. The accuracy depends sensitive on the sensor array configuration and signal processing. Nevertheless, its core principles can be transferred from small to large scale. These findings open the way for further development for structural health monitoring systems based on the TR of AE signals, particularly in the maritime and offshore sectors.

6.2. Recommendations for Future Work

This work has demonstrated the feasibility of using tTR of GUW for impact localization in steel plates and stiffened panels that representative of ship structures. Building on these findings, several promising directions can be pursued to further develop the methodology and expand the areas of applicability.

6.2.1. Extension to Composite Materials

A natural extension of this work is the application of TR based localization to composite materials, which are increasingly gaining ground in the marine and offshore sectors due to their high strength to weight ratio and corrosion resistance. Impacts are of particular interest in composite structures since even Barely Visible Impact Damage (BVID), meaning dents that cannot be identified by eye, lead to significant strength degradation making their early detection crucial [21]. Additionally, AE are not only emitted by impacts but also from other damage events such as delamination, fiber breakage and matrix cracking and with the appropriate sensors the localization of these defects is possible.

To adapt the current methodology to composite structures it must be modified to reflect the material specific guided wave behavior. In isotropic materials, localization using a single guided wave mode, such as A0, is found to be sufficient. However, in composite structures, due to anisotropy and more complex dispersion characteristics may require the use of multi mode localization approaches.

The propagation model used in this research can be extended and implemented in such structures by experimentally estimating material damping and by employing directional wave number $k(\theta, \omega)$ to reflect the anisotropic properties of the material

6.2.2. Impact Severity Assessment and Force Reconstruction

While this work focused on localization, the complete impact identification framework should also be able to assess the severity of impacts. This can be achieved by utilizing the known instrumented hammer force time signals and corresponding sensor responses measured by the PZT sensors during the controlled impact experiments.

The instrumented hammer and the PZT sensors have their own transfer functions and sensitivity. By analyzing the system as a whole, it is possible to determine a transfer function that relates the known impact force to the recorded sensor response.

Utilizing deconvolution, the influence of the impact location and wave propagation path can be decoupled, allowing the construction of a model that maps sensor readings to impact force characteristics. This model, once trained on known impact events, could be then extended to estimate the severity of unknown impacts in similar structural configurations.

References

[1] Agnes Marie Horn. "PSA STUDY STRUCTURAL HEALTH MONITORING OF OFFSHORE STRUCTURE BY USE OF SENSOR DATA Petroleumstilsynet". In: (2024). ISSN: 2023-1241. URL: www.dnv.com.

[2] Archana Nair and C. Cai. "Acoustic emission monitoring of bridges: Review and case studies". In: *Engineering Structures* 32 (June 2010), pp. 1704–1714. DOI: 10.1016/j.engstruct.2010.02.020.

[3] *Monitoring Structural Integrity of North Sea Production Platforms by Acoustic Emission*. Vol. All Days. OTC Offshore Technology Conference. May 1992, OTC-6957–MS. DOI: 10.4043/6957-MS. eprint: https://onepetro.org/OTCONF/proceedings-pdf/92OTC/All-92OTC/OTC-6957-MS/1987271/otc-6957-ms.pdf. URL: https://doi.org/10.4043/6957-MS.

[4] Pooria L Pahlavan. *Acoustic Emission Health Monitoring of Steel Bridges*. 2014. URL: https://www.researchgate.net/publication/281076743.

[5] Sarjoon Alkhateeb et al. "Non-Contact Acoustic Emission Monitoring of Corrosion under Marine Growth". In: *Sensors* 23 (1 Jan. 2023). ISSN: 14248220. DOI: 10.3390/s23010161.

[6] C U Grosse. *Acoustic emission localization methods for large structures based on beamforming and array techniques*. 2009. URL: https://www.ndt.net/?id=7662.

[7] Paul Fromme. "Guided Wave Testing". In: *Handbook of Advanced Nondestructive Evaluation*. Ed. by Nathan Ida and Norbert Meyendorf. Cham: Springer International Publishing, 2019, pp. 141–170. ISBN: 978-3-319-26553-7. DOI: 10.1007/978-3-319-26553-7_24. URL: https://doi.org/10.1007/978-3-319-26553-7_24.

[8] James F. Doyle. "Wave Propagation in Structures: Spectral Analysis Using Fast Discrete Fourier Transforms". In: 1997. URL: https://api.semanticscholar.org/CorpusID:118547340.

[9] V. Giurgiutiu. *Structural Health Monitoring with Piezoelectric Wafer Active Sensors*. Academic Press, 2014. ISBN: 9780124201026. URL: https://books.google.nl/books?id=JyBuAwAAQBAJ.

[10] Debdyuti Mandal and Sourav Banerjee. "Surface Acoustic Wave (SAW) Sensors: Physics, Materials, and Applications". In: *Sensors* 22 (Jan. 2022), p. 820. DOI: 10.3390/s22030820.

[11] Z. Su and L. Ye. *Identification of Damage Using Lamb Waves: From Fundamentals to Applications*. Lecture Notes in Applied and Computational Mechanics. Springer London, 2009. ISBN: 9781848827844. URL: https://books.google.nl/books?id=jvzkoGBwBl0C.

[12] Gregory C. McLaskey, Steven D. Glaser, and Christian U. Grosse. "Beamforming array techniques for acoustic emission monitoring of large concrete structures". In: *Journal of Sound and Vibration* 329 (12 June 2010), pp. 2384–2394. ISSN: 0022460X. DOI: 10.1016/j.jsv.2009.08.037.

[13] Niamat Ullah, Zahoor Ahmed, and Jong Myon Kim. "Pipeline Leakage Detection Using Acoustic Emission and Machine Learning Algorithms". In: *Sensors* 23 (6 Mar. 2023). ISSN: 14248220. DOI: 10.3390/s23063226.

[14] Zhengyan Yang et al. *A review in guided-ultrasonic-wave-based structural health monitoring: From fundamental theory to machine learning techniques*. Aug. 2023. DOI: 10.1016/j.ultras.2023.107014.

[15] Zahra Sharif Khodaei and M.H. Aliabadi. "Impact Detection and Identification with Piezoceramic Sensors: Passive Sensing". In: Jan. 2018, pp. 215–265. ISBN: 978-1-78634-392-5. DOI: 10.1142/9781786343932_0007.

[16] F. Ciampa and M. Meo. "Acoustic emission source localization and velocity determination of the fundamental mode A0 using wavelet analysis and a Newton-based optimization technique". In: *Smart Materials and Structures* 19 (4 2010). ISSN: 09641726. DOI: 10.1088/0964-1726/19/4/045027.

[17] Asaad Migot and Victor Giurgiutiu. "Impact Localization using Sparse PWAS Networks and Wavelet Transform". In: Sept. 2017. DOI: 10.12783/shm2017/13891.

[18] Paul D. Wilcox. "A rapid signal processing technique to remove the effect of dispersion from guided wave signals". In: *IEEE Transactions on Ultrasonics, Ferroelectrics, and Frequency Control* 50 (4 Apr. 2003), pp. 419–427. ISSN: 08853010. DOI: 10.1109/TUFFC.2003.1197965.

[19] Krzysztof Grabowski et al. "Time–distance domain transformation for Acoustic Emission source localization in thin metallic plates". In: *Ultrasonics* 68 (2016), pp. 142–149. ISSN: 0041-624X. DOI: https://doi.org/10.1016/j.ultras.2016.02.015. URL: https://www.sciencedirect.com/science/article/pii/S0041624X16000408.

[20] Arnaud Huijer, Christos Kassapoglou, and Lotfollah Pahlavan. "Acoustic Emission Source Localization in Fiber-Reinforced Composites based on Multimodal Dispersion Compensation of Guided Waves". In: *Proceedings of the 14th International Workshop on Structural Health Monitoring (IWSHM 2023)*. Ed. by Saman Farhangdoust, Alfredo Guemes, and Fu-Kuo Chang. DEStech Publications, 2023, pp. 1192–1199. DOI: 10.12783/shm2023/36860.

[21] Zexing Yu et al. "Locating of acoustic emission source for stiffened plates based on stepwise time-reversal processing with time-domain spectral finite element simulation". In: *Structural Health Monitoring* 22 (2 Mar. 2023), pp. 927–947. ISSN: 17413168. DOI: 10.1177/14759217221094462.

[22] Marco Miniaci et al. "Application of a laser-based time reversal algorithm for impact localization in a stiffened aluminum plate". In: *Frontiers in Materials* 6 (Mar. 2019). ISSN: 22968016. DOI: 10.3389/fmats.2019.00030.

[23] Ros Kiri Ing et al. "In solid localization of finger impacts using acoustic time-reversal process". In: *Applied Physics Letters* 87 (20 Nov. 2005), pp. 1–3. ISSN: 00036951. DOI: 10.1063/1.2130720.

[24] Byeongjin Park et al. "Impact localization in complex structures using laser-based time reversal". In: *Structural Health Monitoring* 11 (5 Sept. 2012), pp. 577–588. ISSN: 14759217. DOI: 10.1177/1475921712449508.

[25] F. Ciampa and M. Meo. "Impact detection in anisotropic materials using a time reversal approach". In: *Structural Health Monitoring* 11 (1 Jan. 2012), pp. 43–49. ISSN: 14759217. DOI: 10.1177/1475921710395815.

[26] Pooria Pahlavan. *Wave Propagation in Thin-walled Composite Structures: Application to Structural Health Monitoring*. 2012.

[27] Zexing Yu et al. "Impact localization and force reconstruction for composite plates based on virtual time reversal processing with time-domain spectral finite element method". In: *Structural Health Monitoring* 22 (6 Nov. 2023), pp. 4149–4170. ISSN: 17413168. DOI: 10.1177/14759217231164297.

[28] M. Ghajari, Z. Sharif Khodaei, and M. H. Aliabadi. "Impact detection using artificial neural networks". In: *Key Engineering Materials*. Vol. 488-489. Trans Tech Publications Ltd, 2012, pp. 767–770. ISBN: 9783037852187. DOI: 10.4028/www.scientific.net/KEM.488-489.767.

[29] Md. Hossain et al. "Antipyretic, analgesic and anti-inflammatory activity of the methanol Mimosa himalayana extract". In: *International Journal of Medicine* 5 (1 Mar. 2017), p. 87. DOI: 10.14419/ijm.v5i1.7331.

[30] Li Yang and Feiyun Xu. "A Novel Acoustic Emission Sources Localization and Identification Method in Metallic Plates Based on Stacked Denoising Autoencoders". In: *IEEE Access* 8 (2020), pp. 141123–141142. ISSN: 21693536. DOI: 10.1109/ACCESS.2020.3012521.

[31] Cong Han et al. "The research on propagation characteristics of acoustic emission signals in stiffened plates based on the multipath propagation model". In: *Ultrasonics* 108 (Dec. 2020). ISSN: 0041624X. DOI: 10.1016/j.ultras.2020.106177.

[32] Alessandro De Luca et al. "Numerical investigation on guided waves dispersion and scattering phenomena in stiffened panels". In: *Materials* 15 (1 Jan. 2022). ISSN: 19961944. DOI: 10.3390/ma15010074.

[33] Cecilia Saccone and Lotfollah Pahlavan. "Influence of stiffeners on acoustic emission monitoring of ship structures". In: *11th European Workshop on Structural Health Monitoring, EWSHM 2024*. NDT.net, 2024. DOI: 10.58286/29587.

[34] Shuyu Wang et al. "Analysis and experimentation of lamb wave transmission characteristics in the stiffened plates". In: *Nondestructive Testing and Evaluation* (Nov. 2024), pp. 1–22. ISSN: 1058-9759. DOI: 10.1080/10589759.2024.2434700. URL: https://www.tandfonline.com/doi/full/10.1080/10589759.2024.2434700.

[35] Chunlin Chen and Fuh Gwo Yuan. "Impact source identification in finite isotropic plates using a time-reversal method: Theoretical study". In: *Smart Materials and Structures* 19 (10 Oct. 2010). ISSN: 09641726. DOI: 10.1088/0964-1726/19/10/105028.

[36] Tadeusz Uhl. "The inverse identification problem and its technical application". In: *Archive of Applied Mechanics*. Vol. 77. May 2007, pp. 325–337. DOI: 10.1007/s00419-006-0086-9.

[37] Mathias Fink. *Time Reversal of Ultrasonic Fields-Part I: Basic Principles*. 1992.

[38] Buli Xu and Victor Giurgiutiu. "Single mode tuning effects on lamb wave time reversal with piezoelectric wafer active sensors for structural health monitoring". In: *Journal of Nondestructive Evaluation* 26 (2-4 Dec. 2007), pp. 123–134. ISSN: 01959298. DOI: 10.1007/s10921-007-0027-8.

[39] Mathias Fink et al. "Time-reversed acoustics". In: *Reports on Progress in Physics* 63.12 (Dec. 2000), p. 1933. DOI: 10.1088/0034-4885/63/12/202. URL: https://dx.doi.org/10.1088/0034-4885/63/12/202.

[40] Augustinus Johannes Berkhout. *Seismic Migration: Imaging of Acoustic Energy by Wave Field Extrapolation..: Imaging of Acoustic Energy by Wave Field Extrapolation*. Elsevier, 2012.

[41] Lotfollah Pahlavan and Gerrit Blacquière. "Fatigue crack sizing in steel bridge decks using ultrasonic guided waves". In: *NDT and E International* 77 (Jan. 2016), pp. 49–62. ISSN: 09638695. DOI: 10.1016/j.ndteint.2015.09.006.

[42] Jian Cai, Lihua Shi, and Xinlin P. Qing. *Erratum: A time-distance domain transform method for Lamb wave dispersion compensation considering signal waveform correction (Smart Materials and Structures (2013) 22)*. Nov. 2013. DOI: 10.1088/0964-1726/22/11/119601.

[43] H.J. Rindorf. *Acoustic Emission Source Location in Theory and in Practice*. Brüel and Kjær technical review. Brüel & Kjær, 1981. URL: https://books.google.nl/books?id=0yzeHAAACAAJ.

[44] Masayasu Ohtsu, Tomoki Shiotani, and Mitsuhiro Shigeishi. "Recommendation of RILEM TC 212-ACD: acoustic emission and related NDE techniques for crack detection and damage evaluation in concrete / Measurement method for acoustic emission signals in concrete". In: *Materials and Structures* 43 (Nov. 2010), pp. 1177–1181. DOI: 10.1617/s11527-010-9638-0.

A

Medium Transfer Function

The methodology for the calculation of the medium transfer function $W(x, \omega)$ is presented. This transfer function describes how an input (impact excitation) propagates through the medium accounting both for dispersion. In this sense $W(x, \omega)$ acts as a Green's function in the frequency domain, describing the system response for a given impact excitation.

The part of the equation that accounts for the propagation of dispersive signals is found according to Doyle [8]. The wave equation in 1D is given by Eq. A.1, however, the same concept holds for the equation of motion of an elastic medium.

$$\frac{\partial^2 u(x,t)}{\partial t^2} = c^2 \nabla^2 u(x,t) \tag{A.1}$$

where, c is the wave speed.

Using the separation of variables, the general solution of the wave propagation problem is obtained.

$$u(x,t) = u(x)e^{i\omega t} \tag{A.2}$$

Substituting into Eq. A.1 results in the following:

$$\frac{\partial^2 u}{\partial x^2} + k^2 u = 0 \tag{A.3}$$

where, $k = \omega / c_p$.

Then, the solution for the forward propagating wave is given by Eq. A.4.

$$u(x,\omega) = Ae^{-ikx} \tag{A.4}$$

Therefore, at any point x in the domain, the displacement field is described according to Eq. A.5

$$u(x,\omega) = A(\omega)e^{-i\frac{\omega x}{c_p}} \tag{A.5}$$

The term $e^{-i\frac{\omega x}{c_p}}$, is in the frequency domain and describes how the dispersive signal propagates in the structure.

The impact spectrum contains various frequencies, therefore, Eq. A.5 should be modified as Eq. A.6 which describes the propagation of each frequency component.

$$u(x,\omega) = \sum_{n} A_n e^{-i\frac{\omega_n x}{c_p}} \tag{A.6}$$

where, A_n is the amplitude spectrum and is calculated using a forward Fast Fourier Transformation (FFT) on the impact signal.

B

Propagation Model Validation

The experiment was designed as shown in Figure B.1. Two Physical Acoustics r6α piezoelectric sensors with 60kHz resonant frequency were used to record the acoustic emissions (AE) emitted by Pencil Lead Breaks (PLB) on the surface of the plate. The signals where recorded by a Vallen Systeme AMSY-6 Data Acquisition System (DAS). The DAS operated in Normal trigger mode, meaning that the recording starts one the signals exceed a predefined threshold, which is based on the background noise level and was set at 30 dB. The pre-trigger was set to 400 μs and the sampling rate was set at 10 MHz. The total length of the signals is set to 1.6384 ms which corresponds to 16384 samples given the selected sampling rate.

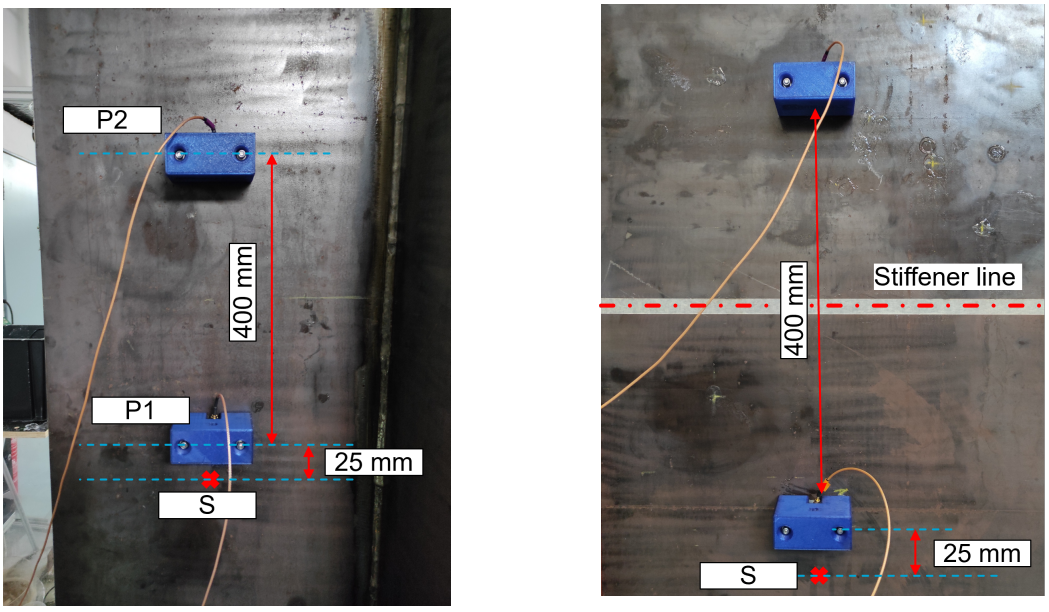

(a) (b)

Figure B.1: Experimental setup used the validation of the propagation model.

Wave mode Identification

The first step before validating the propagation model is to identify the dominant propagating mode. In thin-walled structures, multiple wave modes can propagate simultaneously. In the frequency range of interest of this work, the possible propagating modes are the fundamental symmetric (S0) and antisymmetric (A0) modes. The sensitivity of the sensors to detect each of these modes is critical for accurate modeling.

In this experiment A0 and S0 waves were expected to propagate simultaneously. These modes have

different group speed, but since the distance between the two sensors is short, full separation of the modes is not expected. Figure B.2a, illustrates the first 600 μs of the raw signals recorded by sensor P1 and P2, after alignment in time. One may notice that in Channel 3 two components are visible. Figure B.2b depicts the signals after windowing and filtering.

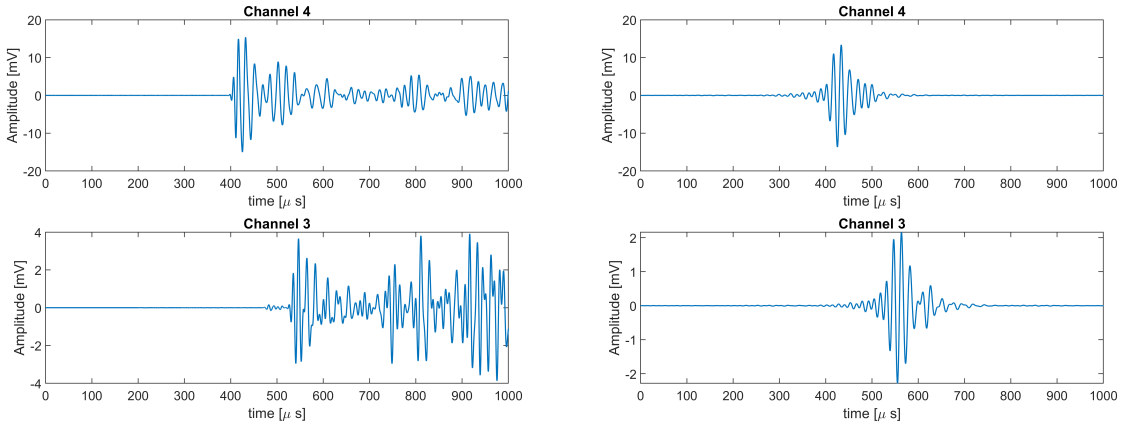

Figure B.2: Experimental setup used the validation of the propagation model.

The mode identification approach is based on the calculation of the group speed of the dominant propagating wave packet. With known distance between the sensors the group velocity is calculated as the division between the distance and the time of arrival difference of the signal to the sensors.

To compute the relative time difference the timestamps of the zero crossing immediately before the peak are used. Figure B.3a shows the processed signals at the position of the sensors. By calculating the slope of the line connecting the zero crossings preceding the maximum amplitude one can identify the group velocity. The group velocity for the frequency range of interest is found as in Equation B.1.

$$c_g = \frac{d}{\Delta t} = 3076.2 \quad [m/s] \tag{B.1}$$

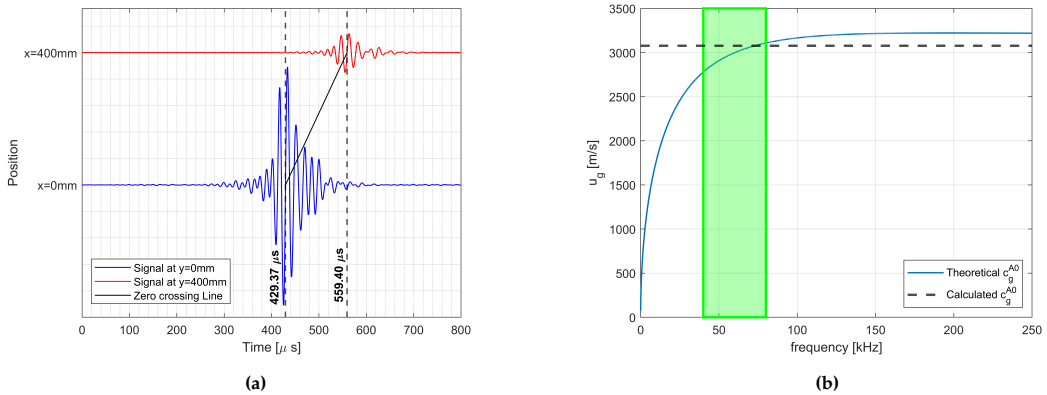

Figure B.3: (a) Pre-processed signals at sensor positions with line connecting the zero crossings. (b) theoretical A0 group velocity

In Figure B.3b the calculated velocity is plotted along the theoretical A0 group speed. It is obvious that the calculated group velocity agrees with the theoretical in the frequency range of interest. Therefore, the assumption that the sensors are more sensitive to A0 wave mode can be made.

Validation of Analytical Wave Propagation model

In this section the validation of the proposed propagation model is described and discussed. The validation is performed using the same experimental set-up as shown in Figure B.1 and can be summarized as follows.

An acoustic emission signal is generated through 0.35 mm PLBs positioned 25mm away from the sensor P1. The signals recorded at sensors P1 and P2 are aligned in time, windowed and filtered, as described in the pre-processing step. The sensors used have 60 kHz resonant frequency, and the applied bandpass filter was centered around that frequency with 40 and 80 kHz being the lower and upper cutoff frequencies respectively, and the filter being flat between 45 and 75 kHz. The signal measured at P1, is considered as the source and was propagated to P2 according to Equation 2.7, when no stiffener is present and according to Equation 2.12 if the wave crosses the stiffener.

The results are shown in Figure B.4.

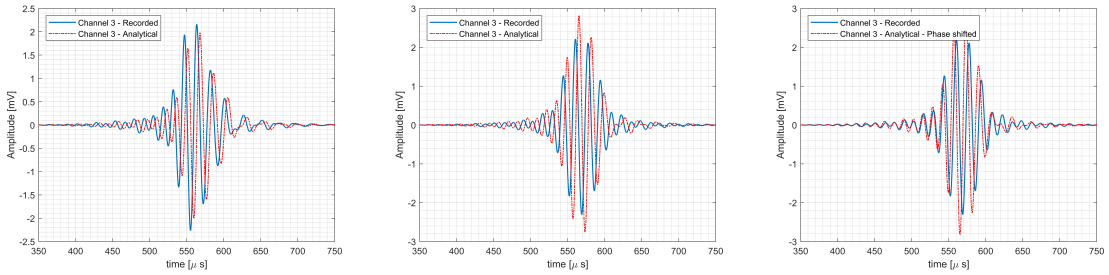

(a) **(b)** **(c)**

Figure B.4: Analytical and recorded wave propagation for: (a) flat plate, (b) stiffened plate, and (c) stiffened plate shifted π rad.

In the case of the flat plate, it is observed that there is a phase offset between the analytical and the recorded signal. This discrepancy may arise from small errors in sensor placement such as misalignment or deviation from the 400 mm spacing, and from the assumption that all the used sensors have identical transfer functions, whereas in practice, each sensor has its own frequency dependent response which may introduce phase variations.

On the stiffened plate, the amplitude attenuation is effectively captured using a scalar transmission coefficient T_c. However, a consistent phase difference of approximately π radians is observed between the analytical and the recorded signals. Figure B.4c depicts the two signals, where the simulated waveform has been shifted by π to align with the measurement. This phase shift, while repeatable in this configuration, cannot be generalized without further investigation. It may depend on several factors such as the relative stiffness of the stiffener to the plate, the incident angle and the wave length of the propagating mode.